

Exploiting Double-Bounce Paths in Snapshot Radio SLAM: Bounds, Algorithms and Experiments

Xi Zhang, *Student Member, IEEE*, Yu Ge, *Member, IEEE*, Ossi Kaltiokallio, *Member, IEEE*,
Musa Furkan Keskin, *Member, IEEE*, Henk Wymeersch, *Fellow, IEEE*, and Mikko Valkama, *Fellow, IEEE*

Abstract—Radio-based simultaneous localization and mapping (SLAM) has the potential to provide precise user equipment (UE) localization and environmental sensing capabilities by exploiting radio signals. Most existing approaches leverage line-of-sight (LoS) and single-bounce non-line-of-sight (NLoS) paths solely, while higher-order NLoS paths are treated as disturbance. In this paper, we investigate the benefits of leveraging double-bounce NLoS paths for solving the bistatic snapshot radio SLAM problem. We derive the Cramér-Rao bound (CRB) for joint estimation of the UE state and landmark positions when double-bounce NLoS paths are present. In addition, we propose an algorithm to identify double-bounce NLoS paths and leverage them into joint UE and landmarks estimation. The derived bounds are validated through simulated data, and the proposed algorithms are evaluated using experimental millimeter wave (mmWave) measurements harnessing beamformed 5G cellular reference signals. The numerical and experimental results demonstrate that the double-bounce NLoS paths which share at least one incidence point (IP) with the single-bounce NLoS paths improve the estimation accuracy of the UE state and existing IPs of single-bounce NLoS paths. Importantly, exploiting double-bounce NLoS paths enhances environmental mapping capabilities by revealing landmarks that are unobservable with single-bounce NLoS paths alone.

Index Terms—5G, 6G, integrated sensing and communication (ISAC), Cramér-Rao bound (CRB), double-bounce paths, multipath, simultaneous localization and mapping (SLAM), mmWave.

I. INTRODUCTION

Integrated sensing and communication (ISAC) is emerging as one key enabler towards 6G wireless networks, as it jointly offers high data-rate communication and precise sensing capabilities [1]. One promising ISAC application is radio-based simultaneous localization and mapping (SLAM), which leverages radio signals to localize the user equipment (UE) while mapping the surrounding environment [2]. In general, various types of radio signals can be utilized for this purpose, including UWB [3], 5G [4], and future 6G signals [5]. In addition, different sensing configurations are possible, such as monostatic [6], [7], bistatic [8], [9], and multistatic [10], [11]. Among these options, bistatic radio SLAM using cellular networks is particularly appealing. It provides full positioning and mapping functionality with only a single base station (BS), which allows minimal infrastructure and eliminates the need for synchronization across multiple BSs [2], [8], [12], [13].

This work was supported by the ISLANDS project under the EU Horizon Europe (HE) Marie Skłodowska-Curie Actions-Doctoral Networks (MSCA-DN), grant agreement No. 101120544, and by the Swedish Research Council (VR) through the project 6G-PERCEF under Grant 2024-04390.

Xi Zhang, Ossi Kaltiokallio, and Mikko Valkama are with the Department of Electrical Engineering, Tampere University, 33100 Tampere, Finland (e-mails: {xi.zhang, ossi.kaltiokallio, mikko.valkama}@tuni.fi).

Yu Ge, Musa Furkan Keskin, and Henk Wymeersch are with the Department of Electrical Engineering, Chalmers University of Technology, 41296 Gothenburg, Sweden (e-mails: {yuge, furkan, henkw}@chalmers.se).

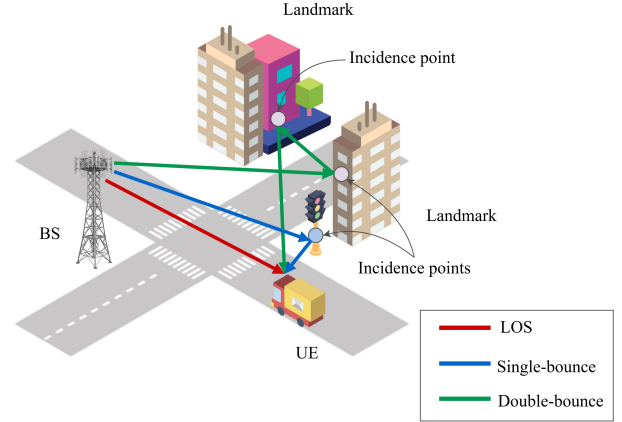


Fig. 1. Illustration of the bistatic radio SLAM problem including LoS, single-bounce, and double-bounce NLoS paths. Double-bounce NLoS paths enable improved environmental sensing capabilities since they can be used to illuminate and detect landmarks and other objects that cannot be observed with single-bounce paths alone.

Radio SLAM algorithms are commonly categorized into snapshot [2], [8], filtering [14], [15], and smoothing [16], [17] based approaches. These categories differ in how they operate over time. Snapshot methods (e.g., least squares (LS) and maximum likelihood estimation (MLE)) [2], [8] solve each epoch independently based on current measurements, without propagating motion estimates, state information, or any prior knowledge forward in time. Filtering methods (e.g., extended Kalman filter (EKF) and particle filter (PF)) [14], [15] perform recursive Bayesian estimation by propagating the filtering density sequentially via time and measurement updates. Smoothing approaches (e.g., GraphSLAM and batch optimization) [16], [17] jointly optimize over a batch of time steps to obtain trajectory estimates. All three approaches rely on signals traveling along the line-of-sight (LoS) path and non-line-of-sight (NLoS) paths, caused by reflections, scattering, and diffraction, to jointly infer the UE state and the positions of environmental landmarks. Most existing works consider only direct LoS and single-bounce NLoS paths, typically assuming that all the NLoS paths are single-bounce paths [18]–[21]. This assumption leads to severe performance degradation when multi-bounce paths are present [8], [22]. Moreover, disregarding multi-bounce paths leaves potential information unexploited, especially in rich multipath environments where higher-order NLoS paths can be strong and geometrically structured [23], [24]. An example scenario is illustrated in Fig. 1, where the double-bounce NLoS path encode rich environmental maps.

The fundamental performance limits of UE state estimation in the presence of NLoS paths have been investigated in

[25]–[28]. In [25], a single anchor localization scenario was considered and the Fisher information matrix (FIM) for the UE position and orientation, as well as the NLoS parameters were presented. Similarly, [26] derived the FIM for channel parameters and further obtained a closed-form expression for the FIM of the UE position and orientation by leveraging the geometric relationship between channel parameters and the UE position and orientation. Continuing with this idea, [27] applied a geometric transformation to convert the channel parameter FIM into the FIM of UE position, orientation, and locations of single-bounce incidence points (IPs), and the influence of different UE, BS and IPs geometries was also investigated. Likewise, the effect of the Doppler shift on the FIM as well as difference in uplink and downlink positioning were considered in [28]. Collectively, the above works show that exploiting NLoS components can benefit the UE position and orientation estimation. However, all the analyses above are limited to single-bounce NLoS components, and the mapping performance is not discussed, as positions of IPs are often treated as nuisance parameters.

Exploiting multi-bounce NLoS paths in radio SLAM is non-trivial for two reasons. First, it is difficult to identify which measurements are from single- or multi-bounce paths. Second, the multi-bounce NLoS paths are much more difficult to handle algorithmically and therefore, many existing solutions restrict their models to single-bounce paths only, ignoring multi-bounce components entirely [18]–[20]. Several works focus on identifying single-bounce paths and mitigating multi-bounce paths [8], [22], [29], [30]. In [22], an iterative algorithm based on change detection was proposed to detect single-bounce NLoS paths, which was then used to estimate the UE position and clock bias. In [29], a random sample consensus (RANSAC)-based outlier rejection algorithm was utilized to classify LoS and single-bounce NLoS paths from multi-bounce NLoS paths, and the resulting classification was used for UE localization. Considering both positioning and mapping, [8] proposed a robust snapshot SLAM solution that uses a RANSAC inspired method to identify the LoS and single-bounce NLoS paths, thereby isolating higher-order NLoS outliers. Differently, [30] leveraged a Hough transform-based line detection method to separate LoS and single-bounce NLoS paths from higher-order NLoS paths, to perform the SLAM. These methods improve robustness by isolating multi-bounce paths, but they do not utilize the potential additional information those multi-bounce paths provide.

By contrast, some recent works have considered incorporating double-bounce NLoS paths into mapping with known poses problems and using them to estimate the positions of scattering points [31], [32]. In [31], an initial map and the UE state were first obtained using LoS and single-bounce paths, after which double-bounce paths were exploited to reveal additional scattering points. In [32], a graph-based method was proposed to model single-bounce and double-bounce paths and these paths were leveraged to iteratively estimate scattering points given known UE position. As for SLAM, [33], [34] introduced their methods based on a multipath SLAM framework that modeled each specular surface as a master virtual anchor. In the method, every double-bounce path is treated as two sequential

specular reflections involving two distinct master virtual anchors which are then jointly estimated on a factor graph over time as the UE moves. However, all NLoS paths are modeled as specular reflections, and reflection points lie on assumed planar surfaces. In summary, the influence and potential of versatile multi-bounce NLoS components in radio SLAM beyond plain specular reflections are not well captured in the existing works.

In this paper, we investigate the potential benefits of double-bounce NLoS paths in the snapshot radio SLAM problem. We first derive the CRB for the problem to obtain the lower bounds on the estimation error variances for the UE position, orientation, clock bias, and IP positions in the presence of double-bounce NLoS paths. We also present the FIM analysis and discuss the identifiability conditions of the problem. Furthermore, we develop a snapshot radio SLAM algorithm that exploits LoS, single-bounce NLoS and double-bounce NLoS paths to estimate the unknown UE state and IPs of the single- and double-bounce paths. The devised method does not rely on any prior information of the environmental map nor the UE state and it can operate in mixed LoS/NLoS conditions. Moreover, the method does not assume any specific propagation mechanisms and works for both specular reflection and diffuse scattering, or the combination of them such that a double-bounce path can be reflected by one surface and scattered by another object as it traverses from the transmitter to the receiver.

The main contributions of this paper can be summarized as follows:

- We derive the fundamental performance bounds for the snapshot radio SLAM problem considering LoS, single-bounce, and double-bounce NLoS paths. The FIM analysis reveals that the SLAM problem is identifiable under general geometric conditions when a double-bounce NLoS path shares at least one of its IPs with single-bounce NLoS paths. The FIM analysis also reveals that the double-bounce NLoS paths improve estimation accuracy of the UE and IPs in such conditions.
- Inspired by the FIM analysis, instead of discarding double-bounce NLoS paths and treating them as outliers, we devise a snapshot radio SLAM algorithm that exploits them. The proposed method recycles double-bounce NLoS paths to enhance SLAM performance, turning them from foe to friend.
- We validate the proposed algorithm using real-world mmWave measurement data, showing that it achieves higher estimation accuracy compared to the baseline methods that discard double-bounce NLoS paths. Moreover, the experimental results demonstrate that double-bounce NLoS paths enhance environmental mapping capabilities by revealing landmarks that are unobservable with single-bounce NLoS paths alone.

The rest of this paper is organized as follows. Section II formulates the problem and describes the fundamentals of the system model. The performance bounds for the considered problem are derived in Section III while the proposed snapshot radio SLAM algorithm is introduced in Section IV. The numerical and experimental results are presented in Section V,

and the conclusions are drawn thereafter. Selected technical details are provided in the Appendix.

Notations: Scalars are denoted by normal font (e.g., a), vectors in lowercase bold letters (e.g., \mathbf{a}), and matrices in capital bold letters (e.g., \mathbf{A}). The operations $(\cdot)^\top$, $(\cdot)^{-1}$, $(\cdot)^H$, $|\cdot|$, $\|\cdot\|$ and $\text{diag}(\cdot)$ denote the transpose, inverse, Hermitian transpose, cardinality of a set (or absolute value when applied to a scalar), Euclidean norm, and the diagonal matrix, respectively. A multivariate Gaussian distribution with mean $\boldsymbol{\mu}$ and covariance $\boldsymbol{\Sigma}$ is denoted as $\mathcal{N}(\boldsymbol{\mu}, \boldsymbol{\Sigma})$.

II. PROBLEM FORMULATION

We consider a bi-static 2D (azimuth domain) downlink scenario with a single BS and a single UE, where the BS acts as the transmitter and the UE acts as the receiver. The BS has known position $\mathbf{p}_{\text{BS}} = [x_{\text{BS}}, y_{\text{BS}}]^\top$ and orientation α_{BS} . The UE state is unknown and given by $\mathbf{s} = [\mathbf{p}_{\text{UE}}^\top, \alpha_{\text{UE}}, b_{\text{UE}}]^\top \in \mathbb{R}^4$, where \mathbf{p}_{UE} is the position, α_{UE} the heading, and b_{UE} the clock bias between the unsynchronized UE and BS clocks. The n th unknown landmark position is represented by $\mathbf{m}_n = [x_n, y_n]^\top$ and the N landmarks form a map of the propagation environment. Furthermore, let $\mathbf{z}_i = [\tau_i, \phi_i, \theta_i]^\top$ denote the channel parameter estimate of the i th propagation path, which consists of the time-of-arrival (ToA), angle-of-departure (AoD) and angle-of-arrival (AoA). The existence of the LoS and the number of resolvable NLoS components depends on the problem geometry and communication system parameters, and the set of channel parameter estimates is denoted using $\mathcal{Z} = \{\mathbf{z}_0, \mathbf{z}_1, \dots, \mathbf{z}_M\}$ in which $i = 0$ is reserved for the LoS component and M denotes the number of NLoS paths.

It is to be importantly noted that in general, it is also unknown whether \mathbf{z}_i is the LoS, single-bounce, double-bounce or higher-order NLoS path, or clutter due to failure in the channel estimation routine. This paper aims to provide theoretical insights into double-bounce snapshot SLAM via FIM analysis, as well as, devising a snapshot radio SLAM algorithm that jointly estimates the UE state and landmark positions using the elements of \mathcal{Z} that correspond to LoS, single-bounce NLoS and double-bounce NLoS.

A. Signal Model

The BS transmits mmWave downlink reference signals to the UE using orthogonal frequency division multiplexing (OFDM). A concrete practical example is the positioning reference signal (PRS) defined in the 3GPP 5G NR standard. Both the BS and UE employ antenna arrays with beamforming. Subcarriers are indexed by k , OFDM symbols by l , BS transmit beams by p , and UE receive beams by q . We assume further the OFDM symbols are captured over a time interval in which the channel is assumed constant. For a multipath radio propagation environment with resolvable path index set $\mathcal{I} = \{0, 1, \dots, M\}$, the received sample is of the form [2]

$$y_{k,l}^{p,q} = \sum_{i \in \mathcal{I}} \xi_i G_{\text{BS}}^p(\phi_i) G_{\text{UE}}^q(\theta_i) e^{-j2\pi k \Delta f \tau_i} x_{k,l}^{p,q} + n_{k,l}^{p,q}, \quad (1)$$

where $x_{k,l}^{p,q}$ is the transmitted reference sample, $n_{k,l}^{p,q}$ denotes the additive noise at the UE side, and Δf is the subcarrier spacing. In the above, the complex path gain, ToA, AoD,

and AoA of the i th propagation path are ξ_i , τ_i , ϕ_i , and θ_i , respectively, and $i = 0$ is reserved for the LoS path. Furthermore, $G_{\text{BS}}^p(\phi) = \mathbf{a}_{\text{BS}}^H(\phi) \mathbf{w}_p$ and $G_{\text{UE}}^q(\theta) = \mathbf{w}_q^H \mathbf{a}_{\text{UE}}(\theta)$ denote the angular responses, including the steering vectors at the BS $\mathbf{a}_{\text{BS}}(\phi)$ and UE $\mathbf{a}_{\text{UE}}(\theta)$, and p th BS beamformer \mathbf{w}_p , q th UE beamformer \mathbf{w}_q .

Various channel parameter estimation methods can be used to recover \mathcal{Z} from (1) with high accuracy [2], [26], [35]. However, the physical channel parameter estimation is outside the main scope of this paper and it is thus assumed that \mathcal{Z} is readily available. Since \mathcal{Z} is used as a measurement input to radio SLAM, the channel parameter estimates are referred to as measurements from now on.

B. Geometric Measurement Model

Let us consider the channel parameter measurement of the i th path, $\mathbf{z}_i = [\tau_i, \phi_i, \theta_i]^\top$, and let us denote the IPs of the path using set $\mathcal{M}_i = \{\mathbf{m}_i^1, \mathbf{m}_i^2, \dots, \mathbf{m}_i^m\}$ which consists of m physical interactions with the environment ($\mathcal{M}_0 = \emptyset$ for the LoS path). Assuming that the measurement noise is zero-mean Gaussian, which is a common assumption in radio SLAM [2], [21], the likelihood function is given by

$$p(\mathbf{z}_i | \mathbf{s}, \mathcal{M}_i) = \mathcal{N}(\mathbf{z}_i; \mathbf{h}_i(\mathbf{s}, \mathcal{M}_i), \mathbf{R}_i), \quad (2)$$

where $\mathbf{R}_i = \text{diag}([\sigma_\tau^2, \sigma_\phi^2, \sigma_\theta^2])$ is the covariance matrix and the mean is given by [8], [31]

$$\mathbf{h}_i(\mathbf{s}, \mathcal{M}_i) = \begin{bmatrix} d_i/c + b_{\text{UE}} \\ \text{atan2}(-\delta_{\phi,i}^y, -\delta_{\phi,i}^x) - \alpha_{\text{BS}} \\ \text{atan2}(\delta_{\theta,i}^y, \delta_{\theta,i}^x) - \alpha_{\text{UE}} \end{bmatrix} \quad (3)$$

in which c is the speed of light and $\text{atan2}(y, x)$ is the two argument arctangent. The mean represents the geometric connection among the BS, UE and \mathcal{M}_i . The parameters of the model in (3) for LoS, single-bounce NLoS and double-bounce NLoS are defined in Appendix A. Higher-order NLoS paths ($m \geq 3$) are not detailed here as they are not used for estimating the UE state and IPs.

III. PERFORMANCE BOUNDS FOR DOUBLE-BOUNCE SNAPSHOT SLAM

In this section, we present the performance bounds for the snapshot SLAM problem considering LoS, single-bounce, and double-bounce paths. Subsequently, we derive the corresponding FIM and analyze the impact of incorporating double-bounce paths in the presence of LoS and single-bounce paths.

A. Performance Bounds

The CRB states that the mean square error (MSE) of an unbiased estimator is always larger than the inverse of the FIM in the positive semi-definite sense [36, Ch. 4.2]. For notational convenience, let us assume the LoS path exists¹ and that $d_s = \dim(\mathbf{s})$, $d_m = \dim(\mathbf{m}_n)$ and $d_z = \dim(\mathbf{z}_i)$ denote the UE, IP and measurement dimensions, respectively. Furthermore, let $\mathbf{x} = [\mathbf{s}^\top, \mathbf{m}_1^\top, \dots, \mathbf{m}_N^\top]^\top \in \mathbb{R}^{(d_s + Nd_m) \times 1}$ denote the joint state of the UE and N landmarks with dimension $d_x = \dim(\mathbf{x})$, and $\mathbf{z} = [\mathbf{z}_0^\top, \mathbf{z}_1^\top, \dots, \mathbf{z}_M^\top]^\top \in \mathbb{R}^{(M+1)d_z \times 1}$

¹This assumption is made for analytical convenience. The derived performance bounds can be extended naturally to LoS absent cases and the unknown parameters are identifiable if a sufficient number of single-bounce NLoS paths are available.

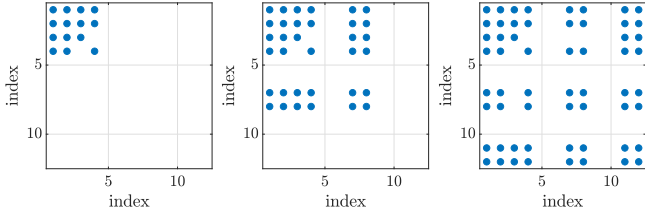


Fig. 2. Visualization of $\mathbf{J}_i(\mathbf{x})$ in (8) for different path types. LoS path visualized on the left ($i \in \mathcal{I}_{\text{LoS}}$, $\mathcal{M}_i = \emptyset$), single-bounce path in the middle ($i \in \mathcal{I}_{\text{SB}}$, $\mathcal{M}_i = \{\mathbf{m}_2\}$), and double-bounce path shown on the right ($i \in \mathcal{I}_{\text{DB}}$, $\mathcal{M}_i = \{\mathbf{m}_2, \mathbf{m}_4\}$). In the example, there are four IPs overall ($N = 4$) and the non-zero elements of $\mathbf{J}_i(\mathbf{x})$ are illustrated using blue markers.

denote the concatenated measurement vector. In the following, we assume the order and index of elements in \mathcal{M}_i are known for every \mathbf{z}_i .² The estimation error CRB has the form [38, Ch. 3.4]

$$\mathbb{E}[(\mathbf{x} - \hat{\mathbf{x}}(\mathbf{z}))(\mathbf{x} - \hat{\mathbf{x}}(\mathbf{z}))^\top] \succeq \mathbf{J}(\mathbf{x})^{-1}, \quad (4)$$

where $\hat{\mathbf{x}}(\mathbf{z})$ denotes an estimator of \mathbf{x} and $\mathbf{J}(\mathbf{x})$ is the $d_{\mathbf{x}} \times d_{\mathbf{x}}$ FIM with elements

$$[\mathbf{J}(\mathbf{x})]_{i,j} = \mathbb{E} \left[-\frac{\partial^2 \log p(\mathbf{z} | \mathbf{x})}{\partial \mathbf{x}_i \partial \mathbf{x}_j} \right] \quad i, j = 1, \dots, d_{\mathbf{x}}, \quad (5)$$

where $p(\mathbf{z} | \mathbf{x})$ denotes the joint likelihood function. After the FIM is computed as explained above, the position error bound (PEB), orientation error bound (OEB), clock bias error bound (BEB), landmark error bound (LEB) of n th landmark, can be computed as: $\text{PEB} = ([(\mathbf{J}(\mathbf{x}))^{-1}]_{1,1} + [(\mathbf{J}(\mathbf{x}))^{-1}]_{2,2})^{1/2}$, $\text{HEB} = ([(\mathbf{J}(\mathbf{x}))^{-1}]_{3,3})^{1/2}$, $\text{BEB} = ([(\mathbf{J}(\mathbf{x}))^{-1}]_{4,4})^{1/2}$, and $\text{LEB}_n = (\sum_{i=2n+3}^{2n+4} [(\mathbf{J}(\mathbf{x}))^{-1}]_{i,i})^{1/2}$.

B. FIM for the Snapshot SLAM

The FIM defined in (5) can be written as [38, Ch. 3.9]

$$\mathbf{J}(\mathbf{x}) = \mathbf{H}(\mathbf{x})^\top \mathbf{R}^{-1} \mathbf{H}(\mathbf{x}), \quad (6)$$

where $\mathbf{H}(\mathbf{x}) = \partial \mathbf{h}(\mathbf{x}) / \partial \mathbf{x} \in \mathbb{R}^{(M+1)d_{\mathbf{z}} \times d_{\mathbf{x}}}$ is the Jacobian of the concatenated measurement model $\mathbf{h}(\mathbf{x}) = [\mathbf{h}_0(\mathbf{s}, \mathcal{M}_0)^\top, \mathbf{h}_1(\mathbf{s}, \mathcal{M}_1)^\top, \dots, \mathbf{h}_M(\mathbf{s}, \mathcal{M}_M)^\top]^\top \in \mathbb{R}^{(M+1)d_{\mathbf{z}} \times 1}$ and $\mathbf{R} = \text{blkdiag}(\mathbf{R}_0, \mathbf{R}_1, \dots, \mathbf{R}_M)$ is the block-diagonal covariance matrix.³ Since the measurements are assumed independent and thus the Fisher information is additive over the paths, $\mathbf{J}(\mathbf{x})$ can be constructed by summing together the FIMs of the individual paths, expressed as

$$\mathbf{J}(\mathbf{x}) = \sum_{i \in \mathcal{I}} \mathbf{J}_i(\mathbf{x}), \quad (7)$$

where the FIM of the i th propagation path is given by

$$\mathbf{J}_i(\mathbf{x}) = \mathbf{H}_i(\mathbf{x})^\top \mathbf{R}_i^{-1} \mathbf{H}_i(\mathbf{x}), \quad (8)$$

in which $\mathbf{H}_i(\mathbf{x}) = \partial \mathbf{h}_i(\mathbf{x}) / \partial \mathbf{x} \in \mathbb{R}^{d_{\mathbf{z}} \times d_{\mathbf{x}}}$. It should be noted that the set of measurement indices is the union of the disjoint LoS, single-bounce and double-bounce index sets, that is, $\mathcal{I} =$

²This assumption is reasonable when deriving the lower bounds on estimation accuracy since we are interested in the best achievable accuracy obtained with perfect data association. We also note that similar assumptions are typically made when computing the CRB [15], [37], and the estimator developed in Section IV does not assume the elements in \mathcal{M}_i , nor the order, are known.

³The block-diagonal structure of \mathbf{R} encodes the assumption that the measurements from different paths are uncorrelated. In practice, correlations may exist, and ignoring them discards some information. This assumption is adopted here to enable a tractable analysis of the considered problem.

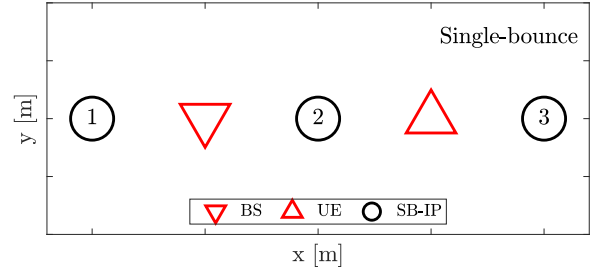


Fig. 3. Examples of rank-deficient single-bounce SLAM geometries. In the examples, the LoS is assumed to exist and one single-bounce IP is considered such that $\dim(\mathbf{x}) = 6$. In scenario 1, as indicated by the number inside the marker, the rank of the FIM is $\text{rank}(\mathbf{J}(\mathbf{x})) = 5$ and null space of the system is $\text{null}(\mathbf{H}(\mathbf{x})) = [-1 \ 0 \ 0 \ 1 \ 0 \ 0]^\top$ meaning that we can change the x coordinate of the UE and the clock bias (in equal but opposite values) without changing the measurements. In scenario 2, $\text{rank}(\mathbf{J}(\mathbf{x})) = 5$ and $\text{null}(\mathbf{H}(\mathbf{x})) = [1 \ 0 \ 0 \ -1 \ 1 \ 0]^\top$, whereas in scenario 3, $\text{rank}(\mathbf{J}(\mathbf{x})) = 4$ and $\text{null}(\mathbf{H}(\mathbf{x})) = \begin{bmatrix} -1 & 0 & 0 & 1 & 0 & 0 \\ 0 & 0 & 0 & 0 & 1 & 0 \end{bmatrix}^\top$.

$\mathcal{I}_{\text{LoS}} \cup \mathcal{I}_{\text{SB}} \cup \mathcal{I}_{\text{DB}}$. The structure of $\mathbf{J}_i(\mathbf{x})$ for different path types is illustrated in Fig. 2 as an example.

C. FIM for Single-bounce Snapshot SLAM

When considering only the LoS and single-bounce paths, the FIM of the problem can be written as

$$\tilde{\mathbf{J}}(\mathbf{x}) = \begin{bmatrix} \tilde{\mathbf{J}}_{\text{ss}} & \tilde{\mathbf{J}}_{\text{sm}} \\ \tilde{\mathbf{J}}_{\text{sm}}^\top & \tilde{\mathbf{J}}_{\text{mm}} \end{bmatrix}. \quad (9)$$

Block $\tilde{\mathbf{J}}_{\text{ss}}$ contains the information contributed to the UE state, $\tilde{\mathbf{J}}_{\text{mm}}$ is the information about the IPs observed from single-bounce paths, and $\tilde{\mathbf{J}}_{\text{sm}}$ captures the coupling between the UE and IPs in the measurement. Let $\mathbf{e}_i \in \mathbb{N}^{|\mathcal{I}_{\text{SB}}| \times 1}$ denote an all-zeros vector with a 1 in the i th element and let $\mathbf{E}_i = \text{diag}(\mathbf{e}_i)$ denote an indicator matrix. Now, the sub-blocks in (9) can be computed as

$$\tilde{\mathbf{J}}_{\text{ss}} = \mathbf{H}_0(\mathbf{s})^\top \mathbf{R}_0^{-1} \mathbf{H}_0(\mathbf{s}) + \sum_{i \in \mathcal{I}_{\text{SB}}} \mathbf{H}_i(\mathbf{s})^\top \mathbf{R}_i^{-1} \mathbf{H}_i(\mathbf{s}), \quad (10)$$

$$\tilde{\mathbf{J}}_{\text{sm}} = \sum_{i \in \mathcal{I}_{\text{SB}}} \left(\mathbf{e}_i^\top \otimes \left(\mathbf{H}_i(\mathbf{s})^\top \mathbf{R}_i^{-1} \mathbf{H}_i(\mathbf{m}_i) \right) \right), \quad (11)$$

$$\tilde{\mathbf{J}}_{\text{mm}} = \sum_{i \in \mathcal{I}_{\text{SB}}} \left(\mathbf{E}_i \otimes \left(\mathbf{H}_i(\mathbf{m}_i)^\top \mathbf{R}_i^{-1} \mathbf{H}_i(\mathbf{m}_i) \right) \right), \quad (12)$$

where $\mathbf{H}_0(\mathbf{s})$ is the Jacobian of LoS measurement with respect to the UE state given in (40), $\mathbf{H}_i(\mathbf{s})$ and $\mathbf{H}_i(\mathbf{m}_i)$ are the Jacobians of i th single-bounce measurement with respect to the UE state and its associated IP, given in (41) and (42), respectively.

Note that the LoS path contributes only to $\tilde{\mathbf{J}}_{\text{ss}}$, whereas each single-bounce path contributes to $\tilde{\mathbf{J}}_{\text{ss}}$, $\tilde{\mathbf{J}}_{\text{mm}}$, and the cross-information $\tilde{\mathbf{J}}_{\text{sm}}$ (linking \mathbf{s} and the corresponding \mathbf{m}_n). By analyzing the FIM in (9), several studies have demonstrated that unambiguous UE state estimation is feasible if a sufficient number of single-bounce NLoS paths are available, even if the LoS path is absent [25]–[28]. Furthermore, the single-bounce NLoS paths can provide UE position and orientation information, thereby improving the accuracy of UE state estimation. For the SLAM problem considered in this work and as shown in [8], the problem is solvable with either (i) the LoS and one single-bounce NLoS, or (ii) four single-bounce

NLoS. However, certain geometric configurations can lead to a rank-deficient FIM. Examples of such degenerate geometries are illustrated in Fig. 3, with their corresponding rank and null spaces summarized in the caption. As shown, when the UE, BS, and IP are collinear, some parameters become unobservable as indicated by $\text{null}(\mathbf{H}(\mathbf{x}))$.

D. Impacts of the Double-bounce Path

Now we analyze how the inclusion of a double-bounce path affects the FIM and the observability of the problem. Let us assume that using existing LoS and single-bounce paths, all unknown parameters can be estimated (i.e., $\tilde{\mathbf{J}}(\mathbf{x}) \succ \mathbf{0}$). We then incorporate one additional double-bounce path. The contribution from this path to the FIM can be written as

$$\mathbf{J}_{\text{DB}} = \begin{bmatrix} \mathbf{A} & \mathbf{B} \\ \mathbf{B}^\top & \mathbf{C} \end{bmatrix}, \quad (13)$$

where the matrix \mathbf{A} corresponds to the information that the double-bounce path provides about the parameters already involved in the LoS and single-bounce paths, \mathbf{C} is the information about any additional parameters introduced by the double-bounce path (i.e., IPs that are only observed from the double-bounce path), and \mathbf{B} captures the cross-information between the existing parameters and the parameters introduced solely from the double-bounce path. Consequently, the overall FIM combining all paths can be formed as

$$\mathbf{J}(\mathbf{x}) = \begin{bmatrix} \tilde{\mathbf{J}}(\mathbf{x}) + \mathbf{A} & \mathbf{B} \\ \mathbf{B}^\top & \mathbf{C} \end{bmatrix}. \quad (14)$$

The structure of matrices \mathbf{A} , \mathbf{B} , and \mathbf{C} depends on the geometric relationship between the IPs of the double-bounce path and those already observed via single-bounce paths. To characterize the resulting information gain on the UE state and the existing IPs and observability properties of the overall SLAM problem, we consider three different cases in the following.

1) *Case 1: Double-bounce path shares both IPs with single-bounce paths:* In this scenario, both IPs of the double-bounce path have also been observed through single-bounce paths. Therefore, the double-bounce measurement does not introduce any new unknown parameters. In terms of the FIM, this implies $\mathbf{B} = \emptyset$ and $\mathbf{C} = \emptyset$, and \mathbf{A} can be computed using (8) in which the Jacobian is $\mathbf{H}_i(\mathbf{x}) = \partial \mathbf{h}_i(\mathbf{x}) / \partial \mathbf{x} \in \mathbb{R}^{d_z \times d_x}$. As an example, the Jacobian for the double-bounce path considered in Fig. 2 is given by

$$\mathbf{H}_i(\mathbf{x}) = \begin{bmatrix} \mathbf{H}_i(\mathbf{s}) & \mathbf{0}_{d_z \times d_m} & \mathbf{H}_i(\mathbf{m}_2) & \mathbf{0}_{d_z \times d_m} & \mathbf{H}_i(\mathbf{m}_4) \end{bmatrix}, \quad (15)$$

where $\mathbf{H}_i(\mathbf{s})$, $\mathbf{H}_i(\mathbf{m}_2)$ and $\mathbf{H}_i(\mathbf{m}_4)$ are given in equations (43), (44) and (45), respectively. As illustrated in Fig. 2, \mathbf{A} contains non-zero entries only in rows/columns corresponding to the UE state and the two involved IPs. Since $\mathbf{A} \succeq \mathbf{0}$ and $\mathbf{J}(\mathbf{x}) = \tilde{\mathbf{J}}(\mathbf{x}) + \mathbf{A} \succeq \tilde{\mathbf{J}}(\mathbf{x}) \succ \mathbf{0}$, we have $(\mathbf{J}(\mathbf{x}))^{-1} \preceq (\tilde{\mathbf{J}}(\mathbf{x}))^{-1}$, and thus, for every parameter the corresponding CRB cannot increase.

To summarize, the inclusion of such double-bounce path directly improves the estimation accuracy of the UE state and the two associated IPs. Moreover, it can indirectly improve the estimation accuracy of other single-bounce IPs through their coupling with the UE state. Consequently, the covariance matrix

of all estimated parameters is reduced, even for parameters that are not directly involved in the double-bounce path.

2) *Case 2: Double-bounce path shares one IP with one of the single-bounce paths:* In this case, one IP of the double-bounce path is seen by an existing single-bounce path, and another IP is added which has not been observed before. Let us denote the existing state vector as $\tilde{\mathbf{x}} = [\mathbf{s}^\top, \mathbf{m}_1^\top, \dots, \mathbf{m}_{N-1}^\top]^\top$, and assume the double-bounce path involves one IP \mathbf{m}_{N-1} and one new IP \mathbf{m}_N . In (13), \mathbf{A} , \mathbf{B} and \mathbf{C} are $(d_s + (N-1)d_m) \times (d_s + (N-1)d_m)$, $(d_s + (N-1)d_m) \times d_m$, $d_m \times d_m$ non-zero block matrices, respectively.

To understand the effect of this double-bounce path on estimating the existing parameters $\tilde{\mathbf{x}}$, we consider the equivalent Fisher information matrix (EFIM) of $\tilde{\mathbf{x}}$, which is given as the Schur complement of \mathbf{C} in (14)

$$\mathbf{J}^e = \tilde{\mathbf{J}}(\tilde{\mathbf{x}}) + \mathbf{A} - \mathbf{B}\mathbf{C}^{-1}\mathbf{B}^\top, \quad (16)$$

when \mathbf{C} is invertible. Here, \mathbf{J}^e is composed of three terms. The first term $\tilde{\mathbf{J}}(\tilde{\mathbf{x}})$ quantifies the information from LoS and single-bounce paths. The second term \mathbf{A} quantifies the information gain from the double-bounce path if \mathbf{m}_N were known. And, the third term $\mathbf{B}\mathbf{C}^{-1}\mathbf{B}^\top$ quantifies the loss of information considering the uncertainty of \mathbf{m}_N .

Since \mathbf{J}_{DB} is the information matrix meaning that $\mathbf{J}_{\text{DB}} \succeq \mathbf{0}$. When \mathbf{C} is non-singular, we have $\mathbf{C} \succ \mathbf{0}$. Therefore, the Schur complement of \mathbf{C} satisfies that

$$\mathbf{A} - \mathbf{B}\mathbf{C}^{-1}\mathbf{B}^\top \succeq \mathbf{0}, \quad (17)$$

meaning that the net information gain from the double-bounce path to the existing parameters $\tilde{\mathbf{x}}$ is always non-negative. In other words, adding this double-bounce path cannot degrade the estimation performance of $\tilde{\mathbf{x}}$.

Next, we give the structure of \mathbf{A} , \mathbf{B} and \mathbf{C} , to provide a structure of the term $\mathbf{A} - \mathbf{B}\mathbf{C}^{-1}\mathbf{B}^\top$. Let i be the index of the double-bounce path under consideration. By definition, we can write \mathbf{A} as

$$\mathbf{A} = \mathbf{H}_i(\tilde{\mathbf{x}})^\top \mathbf{R}_i^{-1} \mathbf{H}_i(\tilde{\mathbf{x}}), \quad (18)$$

and the second term in (17) can be expressed as

$$\begin{aligned} \mathbf{B}\mathbf{C}^{-1}\mathbf{B}^\top &= \mathbf{H}_i(\tilde{\mathbf{x}})^\top \mathbf{R}_i^{-1} \mathbf{H}_i(\mathbf{m}_N) \\ &\times \left(\mathbf{H}_i(\mathbf{m}_N)^\top \mathbf{R}_i^{-1} \mathbf{H}_i(\mathbf{m}_N) \right)^{-1} \mathbf{H}_i(\mathbf{m}_N)^\top \mathbf{R}_i^{-1} \mathbf{H}_i(\tilde{\mathbf{x}}), \end{aligned} \quad (19)$$

where $\mathbf{H}_i(\tilde{\mathbf{x}})$ is the Jacobian of the double-bounce measurement with respect to $\tilde{\mathbf{x}}$, which can be expressed as $\mathbf{H}_i(\tilde{\mathbf{x}}) = [\mathbf{H}_i(\mathbf{s}), \mathbf{0}_{d_z \times (N-1)d_m}, \mathbf{H}_i(\mathbf{m}_{N-1})]$. The Jacobians $\mathbf{H}_i(\mathbf{s})$, $\mathbf{H}_i(\mathbf{m}_{N-1})$, and $\mathbf{H}_i(\mathbf{m}_N)$ are given in (43), (44) and (45), respectively. For notational simplicity, let $\tilde{\mathbf{H}}_{i,\tilde{\mathbf{x}}} \triangleq \mathbf{H}_i(\tilde{\mathbf{x}})$, $\tilde{\mathbf{H}}_{i,\mathbf{m}} \triangleq \mathbf{H}_i(\mathbf{m}_N)$. We can perform Cholesky decomposition of \mathbf{R}_i^{-1} such that $\mathbf{R}_i^{-1} = \mathbf{W}^\top \mathbf{W}$ and define $\tilde{\mathbf{H}}_{i,\tilde{\mathbf{x}}} = \mathbf{W}\tilde{\mathbf{H}}_{i,\tilde{\mathbf{x}}}$ and $\tilde{\mathbf{H}}_{i,\mathbf{m}} = \mathbf{W}\tilde{\mathbf{H}}_{i,\mathbf{m}}$. Substituting these into (18) and (19) gives

$$\mathbf{A} = \tilde{\mathbf{H}}_{i,\tilde{\mathbf{x}}}^\top \tilde{\mathbf{H}}_{i,\tilde{\mathbf{x}}}, \quad (20)$$

$$\mathbf{B}\mathbf{C}^{-1}\mathbf{B}^\top = \tilde{\mathbf{H}}_{i,\tilde{\mathbf{x}}}^\top \tilde{\mathbf{H}}_{i,\mathbf{m}} \left(\tilde{\mathbf{H}}_{i,\mathbf{m}}^\top \tilde{\mathbf{H}}_{i,\mathbf{m}} \right)^{-1} \tilde{\mathbf{H}}_{i,\mathbf{m}}^\top \tilde{\mathbf{H}}_{i,\tilde{\mathbf{x}}}. \quad (21)$$

Define next $\mathbf{P} = \tilde{\mathbf{H}}_{i,\mathbf{m}} \left(\tilde{\mathbf{H}}_{i,\mathbf{m}}^\top \tilde{\mathbf{H}}_{i,\mathbf{m}} \right)^{-1} \tilde{\mathbf{H}}_{i,\mathbf{m}}^\top$, which is the orthogonal projector onto the column space of $\tilde{\mathbf{H}}_{i,\mathbf{m}}$. Therefore,

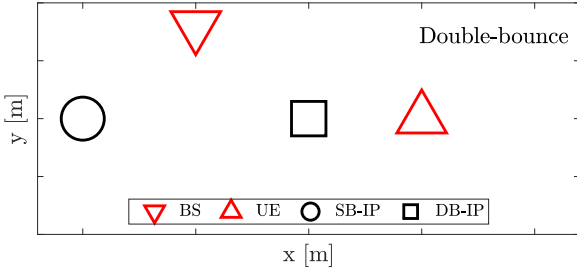


Fig. 4. An example of a rank-deficient double-bounce SLAM geometry. The example considers the LoS, one single-bounce NLoS and one double-bounce NLoS that shares one of the IPs with the single-bounce path. The dimension of the joint state is $\dim(\mathbf{x}) = 8$, the rank of the FIM is $\text{rank}(\mathbf{J}(\mathbf{x})) = 7$ and null space of the system is $\text{null}(\mathbf{H}(\mathbf{x})) = [0 \ 0 \ 0 \ 0 \ 0 \ 0 \ 1 \ 0]^T$.

the difference of interest can be written as

$$\mathbf{A} - \mathbf{B}\mathbf{C}^{-1}\mathbf{B}^T = \tilde{\mathbf{H}}_{i,\tilde{\mathbf{x}}}^T(\mathbf{I} - \mathbf{P})\tilde{\mathbf{H}}_{i,\tilde{\mathbf{x}}}. \quad (22)$$

Since the matrix $\tilde{\mathbf{H}}_{i,\mathbf{m}}$ has full column rank $d_{\mathbf{m}} = 2$, the projection matrix \mathbf{P} is also rank two. Consequently, in (22), the matrix $\mathbf{I} - \mathbf{P}$ is rank one, and the matrix $\tilde{\mathbf{H}}_{i,\tilde{\mathbf{x}}}^T(\mathbf{I} - \mathbf{P})\tilde{\mathbf{H}}_{i,\tilde{\mathbf{x}}}$ is rank one. Therefore, the double-bounce path only provides information in one dimension to the existing parameters $\tilde{\mathbf{x}}$. Intuitively, when \mathbf{m}_N is the last IP before reaching UE, as shown in (45), the Jacobian entries corresponding to the AoD measurement are zero, meaning that \mathbf{m}_N does not influence the AoD, and the AoD directly contributes to $\tilde{\mathbf{x}}$.

It is important to note that the above conclusion holds only if the matrix \mathbf{C} is invertible (full rank). In certain geometric configurations, $\mathbf{H}_i(\mathbf{m}_N)$ may not have full column rank, causing \mathbf{C} to be singular. One such degenerate scenario happens when the \mathbf{m}_{N-1} , \mathbf{m}_N , and the UE are collinear and the \mathbf{m}_N lies between \mathbf{m}_{N-1} and the UE. This is reflected in the Jacobian $\mathbf{H}_i(\mathbf{m}_N)$: under this collinear geometry, the elements in the first row of $\mathbf{H}_i(\mathbf{m}_N)$ become zeros (see the expression in (45)). An example of this rank-deficient geometry is illustrated in Fig. 4, and the resulting FIM rank and null space are detailed in the caption. As shown, moving the second IP (black square) along the x -axis has no effect on the observed measurements, resulting in the x -direction of the second IP becoming unidentifiable.

3) *Case 3: Double-bounce path does not share IPs with any single-bounce paths:* In the third case, both IPs of the double-bounce path are new and have not been observed from any single-bounce paths. Thus, such path introduces two new unknown vectors into the estimation problem. The FIM contribution from the double-bounce in this case has the structure $\mathbf{A} \in \mathbb{R}^{(d_s+(N-2)d_m) \times (d_s+(N-2)d_m)}$, $\mathbf{B} \in \mathbb{R}^{(d_s+(N-2)d_m) \times 2d_m}$ and $\mathbf{C} \in \mathbb{R}^{2d_m \times 2d_m}$. Importantly, the rank of $\mathbf{C} \leq d_z = 3$ is always smaller than the dimension of new involved parameters $2d_m = 4$, and at least one degree of freedom remains unobservable. Thus, \mathbf{C} is rank-deficient, and the resulting overall FIM $\mathbf{J}(\mathbf{x})$ is also rank-deficient. As a result, if both IPs of a double-bounce path have not been unobserved elsewhere, adding this double-bounce path does not provide information gain on the UE and single-bounce IPs. Identifying and discarding such double-bounce path, the SLAM problem can still be solvable.

In summary, under general geometric conditions, adding

double-bounce paths that share at least one IP with single-bounce paths results in a solvable SLAM problem. Moreover, these double-bounce paths can provide information gain on the UE state and all single-bounce IPs, thus improving the estimation accuracy of these parameters. An exceptional rank-deficient geometry case is illustrated in Fig. 4, where adding a double-bounce that shares one IP with a single-bounce path renders the problem unsolvable. In this degenerate case, the double-bounce path can be identified and removed after which the problem remains solvable.

IV. PROPOSED DOUBLE-BOUNCE SNAPSHOT SLAM ALGORITHMS

In this section, we describe the proposed method to solve the snapshot SLAM problem utilizing measurements from the LoS, single-bounce, and double-bounce paths.

A. Proposed Method – High-Level Approach

Recall that $\mathcal{I} = \{0, 1, \dots, M\}$ is the measurement index set which can be partitioned into four disjoint sets as $\mathcal{I} = \{\mathcal{I}_{\text{LoS}}, \mathcal{I}_{\text{SB}}, \mathcal{I}_{\text{DB}}, \mathcal{I}_{\text{HO}}\}$, where \mathcal{I}_{LoS} is the LoS index, \mathcal{I}_{SB} and \mathcal{I}_{DB} contain the single- and double-bounce indices, respectively, and \mathcal{I}_{HO} is the set of indices corresponding to higher-order interactions and clutter measurements, which do not provide any useful information for solving the problem. One of the main difficulties in solving the snapshot SLAM problem is correctly classifying the elements in the disjoint sets. To overcome this challenge, we propose a four-step estimator which can be summarized as follows:

- 1) *Initial SLAM solution* – To compute the initial UE and landmark estimates, we resort to the robust snapshot SLAM algorithm described in [8]. The method partitions the measurements into a set of inliers $\mathcal{I}_{\text{inlier}} = \{\mathcal{I}_{\text{LoS}}, \mathcal{I}_{\text{SB}}\}$ which are used to solve the problem, and outliers $\mathcal{I}_{\text{outlier}} = \{\mathcal{I}_{\text{DB}}, \mathcal{I}_{\text{HO}}\}$ which are considered as unwanted propagation paths that degrade SLAM performance. The method is summarized in Section IV-B.
- 2) *Double-bounce classification* – From the set of outliers $i \in \mathcal{I}_{\text{outlier}}$ obtained in the first step, propagation path i is classified as a double-bounce path based on geometrical consistency with respect to $i' \in \mathcal{I}_{\text{SB}}$. The classification details of \mathcal{I}_{DB} are provided in Section IV-C.
- 3) *Estimating IPs of \mathcal{I}_{DB}* – The identified double-bounce paths share either one or both IPs with the single-bounce paths. If path $i \in \mathcal{I}_{\text{DB}}$ only shares one of the IPs with path $i' \in \mathcal{I}_{\text{SB}}$, the second IP of the double-bounce path can be estimated from the intersection point of a half-line and an ellipse. In Section IV-D, a closed-form solution for the second IP is derived.
- 4) *Double-bounce snapshot SLAM* – The MLE for the double-bounce snapshot SLAM problem is presented in Section IV-E. The devised method utilizes $\{\mathcal{I}_{\text{LoS}}, \mathcal{I}_{\text{SB}}, \mathcal{I}_{\text{DB}}\}$, as well as the initial UE and landmark estimates obtained in steps 1 – 3.

B. Initial SLAM Solution

To solve the SLAM problem in mixed LoS/NLoS conditions, we resort to the robust snapshot SLAM algorithm introduced

initially in [8]. The algorithm uses a RANSAC inspired LS approach in which the method first uses a minimal subset of the channel parameter estimates $\mathcal{Z} = \{\mathbf{z}_0, \mathbf{z}_1, \dots, \mathbf{z}_M\}$ to compute an initial solution $\hat{\mathbf{s}}_0$. Then, based on $\hat{\mathbf{s}}_0$ and an error metric, the measurement indices are partitioned into a set of inliers $\mathcal{I}_{\text{inlier}} = \{\mathcal{I}_{\text{LoS}}, \mathcal{I}_{\text{SB}}\}$ and outliers $\mathcal{I}_{\text{outlier}} = \{\mathcal{I}_{\text{DB}}, \mathcal{I}_{\text{HO}}\}$ such that $\mathcal{I} = \{\mathcal{I}_{\text{inlier}}, \mathcal{I}_{\text{outlier}}\}$, where $\mathcal{I}_{\text{inlier}} \cap \mathcal{I}_{\text{outlier}} = \emptyset$. Thereafter, the problem is re-solved using $\mathcal{I}_{\text{inlier}}$ and the UE estimate $\hat{\mathbf{s}}$ is the one that minimizes the LS cost. Lastly, the map estimate is given by $\hat{\mathcal{M}} = \{\hat{\mathbf{m}}_i \mid i \in \mathcal{I}_{\text{SB}}\}$ in which the landmark estimates $\hat{\mathbf{m}}_i$ are computed independently for every $i \in \mathcal{I}_{\text{SB}}$ by solving a nonlinear optimization problem.

C. Double-bounce Classification

Given the single-bounce index set \mathcal{I}_{SB} identified in Section IV-B, we identify the double-bounce paths $\mathcal{I}_{\text{DB}} \subseteq \mathcal{I}_{\text{outlier}}$ by exploiting angular consistency. Specifically, if a candidate double-bounce path and a single-bounce path share the same IP on the transmitter side, their AoDs are expected to be closely aligned. Or vice versa, if the IP is on the receiver side, their AoAs are expected to be similar.

Let us denote the angular distances between the AoDs and AoAs of the candidate double-bounce path $i \in \mathcal{I}_{\text{outlier}}$ and identified single-bounce paths \mathcal{I}_{SB} using $\delta\phi_i = [\Delta(\phi_i, \phi_1), \dots, \Delta(\phi_i, \phi_{|\mathcal{I}_{\text{SB}}|})]$ and $\delta\theta_i = [\Delta(\theta_i, \theta_1), \dots, \Delta(\theta_i, \theta_{|\mathcal{I}_{\text{SB}}|})]$, respectively, in which the angular distance between two angles is defined as

$$\Delta(a, b) = |(a - b + \pi) \bmod 2\pi - \pi|. \quad (23)$$

Let $\psi_i = [\delta\phi_i, \delta\theta_i]$ denote the combined angular distance vector. The index with the smallest angle error is given by

$$n_\psi = \arg \min_n \psi_i, \quad n = 1, 2, \dots, 2|\mathcal{I}_{\text{SB}}| \quad (24)$$

and if $[\psi_i]_{n_\psi}$ is below angular threshold T_ψ , path i is classified as a double-bounce path. Mathematically, \mathcal{I}_{DB} is formed as follows

$$\mathcal{I}_{\text{DB}} = \{i \in \mathcal{I}_{\text{outlier}} \mid [\psi_i]_{n_\psi} \leq T_\psi\}. \quad (25)$$

D. Estimating IPs of \mathcal{I}_{DB}

The IPs $\mathcal{M}_i = \{\mathbf{m}_i^1, \mathbf{m}_i^2\}$ for double-bounce paths $i \in \mathcal{I}_{\text{DB}}$ are formed by considering two cases:

- 1) *Case 1:* We use IPs of two different single-bounce paths as $\mathcal{M}_i = \{\mathbf{m}_i^1, \mathbf{m}_i^2\}$ if the following logical condition

$$[\delta\phi_i]_{n_\phi} \leq T_\psi \text{ and } [\delta\theta_i]_{n_\theta} \leq T_\psi, \quad (26)$$

is true. In the above, the AoD and AoA indices are given by, $n_\phi = \arg \min_n \delta\phi_i$ and $n_\theta = \arg \min_n \delta\theta_i$, respectively. The IPs of the double-bounce path are $\mathbf{m}_i^1 = \hat{\mathbf{m}}_{n_\phi}$ and $\mathbf{m}_i^2 = \hat{\mathbf{m}}_{n_\theta}$.

- 2) *Case 2:* We use an IP of a single-bounce path as \mathbf{m}_i^1 and the details to estimate \mathbf{m}_i^2 are explained below. If $n_\psi \leq |\mathcal{I}_{\text{SB}}|$, the AoDs of the single- and double-bounce paths are similar and we set $\mathbf{m}_i^1 = \hat{\mathbf{m}}_{n_\psi}$. Conversely, if $n_\psi > |\mathcal{I}_{\text{SB}}|$, the AoAs are similar and we set $\mathbf{m}_i^1 = \hat{\mathbf{m}}_{n_\psi - |\mathcal{I}_{\text{SB}}|}$.

Next, we describe how \mathbf{m}_i^2 is estimated in *Case 2*. The method is inspired by [31] but, differently, a closed-form derivation is given below. Let us denote the starting point, two IPs

and the end point of $i \in \mathcal{I}_{\text{DB}}$ using $\mathcal{P}_i = \{\mathbf{p}_i^0, \mathbf{m}_i^1, \mathbf{m}_i^2, \mathbf{p}_i^3\}$. If the index with the smallest angle error is $n_\psi \leq |\mathcal{I}_{\text{SB}}|$ (see Eq. (24)), BS is considered the starting point ($\mathbf{p}_i^0 = \hat{\mathbf{p}}_{\text{BS}}$) and UE the end point ($\mathbf{p}_i^3 = \hat{\mathbf{p}}_{\text{UE}}$). Or vice versa if $n_\psi > |\mathcal{I}_{\text{SB}}|$, UE is considered the starting point ($\mathbf{p}_i^0 = \hat{\mathbf{p}}_{\text{UE}}$) and BS the end point ($\mathbf{p}_i^3 = \hat{\mathbf{p}}_{\text{BS}}$). The second IP is then located on a half-line

$$\mathbf{m}_i^2 = \mathbf{p}_i^3 + \lambda \mathbf{t}_i, \quad \lambda > 0, \quad (27)$$

that spans from \mathbf{p}_i^3 toward the unit direction vector \mathbf{t}_i , given by

$$\mathbf{t}_i = \begin{cases} \mathbf{\Omega}(\hat{\alpha}_{\text{UE}})[\cos(\theta_i), \sin(\theta_i)]^\top & \text{if } n_\psi \leq |\mathcal{I}_{\text{SB}}|, \\ \mathbf{\Omega}(\alpha_{\text{BS}})[\cos(\phi_i), \sin(\phi_i)]^\top & \text{otherwise,} \end{cases} \quad (28)$$

in which $\mathbf{\Omega}(\alpha) = \begin{bmatrix} \cos(\alpha) & -\sin(\alpha) \\ \sin(\alpha) & \cos(\alpha) \end{bmatrix}$ is a counterclockwise rotation matrix. The second IP also resides on an ellipse defined as

$$\|\mathbf{m}_i^2 - \mathbf{m}_i^1\| + \|\mathbf{m}_i^2 - \mathbf{p}_i^3\| = d_i^e, \quad (29)$$

with $d_i^e = c(\tau_i - \hat{b}_{\text{UE}}) - \|\mathbf{p}_i^0 - \mathbf{m}_i^1\|$ and two foci at \mathbf{m}_i^1 and \mathbf{p}_i^3 . Thus, \mathbf{m}_i^2 is at the intersection point of a half-line and an ellipse, and a closed-form solution can be obtained by combining (27) and (29) and solving for \mathbf{m}_i^2 . This is achieved by first plugging (27) into (29), which gives

$$\|\mathbf{p}_i^3 + \lambda \mathbf{t}_i - \mathbf{m}_i^1\| + \|\mathbf{p}_i^3 + \lambda \mathbf{t}_i - \mathbf{p}_i^3\| = d_i^e. \quad (30)$$

By expanding the Euclidean norms and noting that $\|\mathbf{p}_i^3 + \lambda \mathbf{t}_i - \mathbf{p}_i^3\| = \lambda$ since \mathbf{t}_i is a unit vector, yields

$$\sqrt{\|\mathbf{p}_i^3 - \mathbf{m}_i^1\|^2 + 2\lambda(\mathbf{p}_i^3 - \mathbf{m}_i^1)^\top \mathbf{t}_i + \lambda^2} = d_i^e - \lambda. \quad (31)$$

Taking the square on both sides and solving for λ gives

$$\lambda = \frac{(d_i^e)^2 - \|\mathbf{p}_i^3 - \mathbf{m}_i^1\|^2}{2((\mathbf{p}_i^3 - \mathbf{m}_i^1)^\top \mathbf{t}_i + d_i^e)}, \quad (32)$$

and substituting λ back into (27) yields the closed-form solution

$$\hat{\mathbf{m}}_i^2 = \mathbf{p}_i^3 + \frac{(d_i^e)^2 - \|\mathbf{p}_i^3 - \mathbf{m}_i^1\|^2}{2((\mathbf{p}_i^3 - \mathbf{m}_i^1)^\top \mathbf{t}_i + d_i^e)} \mathbf{t}_i. \quad (33)$$

After solving $\hat{\mathbf{m}}_i^2$, the feasibility of the solution is checked using $d_i^e > \|\mathbf{p}_i^3 - \mathbf{m}_i^1\|$. If the solution is feasible, the IP is appended to the map, as $\hat{\mathcal{M}} = \hat{\mathcal{M}} \cup \hat{\mathbf{m}}_i^2$, and if the check fails, the candidate path i is removed from \mathcal{I}_{DB} , that is, $\mathcal{I}_{\text{DB}} = \mathcal{I}_{\text{DB}} \setminus i$.

E. Double-bounce Snapshot SLAM

Recall that the joint state of the UE and IPs is $\mathbf{x} = [\mathbf{s}^\top, \mathbf{m}_1^\top, \dots, \mathbf{m}_{|\mathcal{M}|}^\top]^\top \in \mathbb{R}^{(d_s + |\mathcal{M}|d_m) \times 1}$ in which $\mathbf{m}_n \in \mathcal{M}$. The considered double-bounce snapshot SLAM problem can be solved by maximizing the joint likelihood function with respect to \mathbf{x} , which is equivalent to minimizing the negative log-likelihood, resulting in the following problem

$$\hat{\mathbf{x}} = \arg \min_{\mathbf{x}} L(\mathbf{x}). \quad (34)$$

In the above, $L(\mathbf{x})$ is the quadratic cost function we wish to minimize and is given by

$$L(\mathbf{x}) = (\mathbf{z} - \mathbf{h}(\mathbf{x}))^\top \mathbf{R}^{-1} (\mathbf{z} - \mathbf{h}(\mathbf{x})). \quad (35)$$

Since the measurements are independent, we can express the cost function as

$$L(\mathbf{x}) = \sum_{i \in \mathcal{I}_{\text{inlier}}} (\mathbf{z}_i - \mathbf{h}_i(\mathbf{x}))^\top \mathbf{R}_i^{-1} (\mathbf{z}_i - \mathbf{h}_i(\mathbf{x})), \quad (36)$$

where the inlier set $\mathcal{I}_{\text{inlier}} = \{\mathcal{I}_{\text{LOS}}, \mathcal{I}_{\text{SB}}, \mathcal{I}_{\text{DB}}\}$ is estimated as explained in Sections IV-B and IV-C. It is important to note that since the data association between measurements and IPs has already been solved in steps 1-3 of the proposed algorithm, it is known which elements of \mathbf{x} correspond to \mathcal{M}_i .

The problem defined above can be solved iteratively, for example, using the Gauss-Newton algorithm, which is based on approximating the measurement model using a first order Taylor series expansion around the linearization point $\hat{\mathbf{x}}^{(j)}$ [39]. The approximation is given by

$$\mathbf{h}_i(\mathbf{x}) \approx \mathbf{h}_i(\hat{\mathbf{x}}^{(j)}) + \mathbf{H}_i(\hat{\mathbf{x}}^{(j)})(\mathbf{x} - \hat{\mathbf{x}}^{(j)}), \quad (37)$$

in which the model $\mathbf{h}_i(\hat{\mathbf{x}}^{(j)}) \in \mathbb{R}^{d_z \times 1}$ and Jacobian $\mathbf{H}_i(\hat{\mathbf{x}}^{(j)}) = \partial \mathbf{h}_i(\mathbf{x}) / \partial \mathbf{x} \in \mathbb{R}^{d_z \times d_x}$ are evaluated at the current linearization point $\hat{\mathbf{x}}^{(j)}$.⁴ The update step of the Gauss-Newton algorithm can be derived by inserting (37) into (36), setting the gradient of $L(\mathbf{x})$ to zero and solving for \mathbf{x} . The gradient is given by

$$\begin{aligned} \frac{\partial L(\mathbf{x})}{\partial \mathbf{x}} &\approx 2 \sum_{i \in \mathcal{I}_{\text{inlier}}} (\mathbf{H}_i(\hat{\mathbf{x}}^{(j)}))^{\top} \mathbf{R}_i^{-1} \mathbf{H}_i(\hat{\mathbf{x}}^{(j)}) (\mathbf{x} - \hat{\mathbf{x}}^{(j)}) \\ &\quad - 2 \sum_{i \in \mathcal{I}_{\text{inlier}}} (\mathbf{H}_i(\hat{\mathbf{x}}^{(j)}))^{\top} \mathbf{R}_i^{-1} (\mathbf{z}_i - \mathbf{h}_i(\hat{\mathbf{x}}^{(j)})), \end{aligned} \quad (38)$$

and solving for \mathbf{x} yields the updated state estimate

$$\begin{aligned} \hat{\mathbf{x}}^{(j+1)} &= \hat{\mathbf{x}}^{(j)} + \left(\sum_{i \in \mathcal{I}_{\text{inlier}}} (\mathbf{H}_i(\hat{\mathbf{x}}^{(j)}))^{\top} \mathbf{R}_i^{-1} \mathbf{H}_i(\hat{\mathbf{x}}^{(j)}) \right)^{-1} \\ &\quad \times \left(\sum_{i \in \mathcal{I}_{\text{inlier}}} (\mathbf{H}_i(\hat{\mathbf{x}}^{(j)}))^{\top} \mathbf{R}_i^{-1} (\mathbf{z}_i - \mathbf{h}_i(\hat{\mathbf{x}}^{(j)})) \right). \end{aligned} \quad (39)$$

The Gauss-Newton algorithm is initialized using the results obtained in steps 1–3 of the proposed double-bounce snapshot SLAM algorithm. The joint state of the UE and IPs is initialized as $\hat{\mathbf{x}}^{(0)} = [\hat{\mathbf{s}}^{\top}, \hat{\mathbf{m}}_1^{\top}, \dots, \hat{\mathbf{m}}_N^{\top}]^{\top}$ in which $\hat{\mathbf{s}}$ is estimated as explained in Section IV-B, $N = |\hat{\mathcal{M}}|$ is cardinality of the map, and $\hat{\mathbf{m}}_n \in \hat{\mathcal{M}}$ represent the IPs of the single and double-bounce paths that are estimated as explained in Sections IV-B and IV-D. The Gauss-Newton algorithm is run iteratively until the norm of the update step falls below a threshold ($\|\hat{\mathbf{x}}^{(j+1)} - \hat{\mathbf{x}}^{(j)}\| < T_e$) or a maximum number of iterations is reached ($j + 1 \geq J$).

V. RESULTS

A. Numerical Evaluations and Insight

1) *Simulation Setup*: The double-bounce SLAM performance bounds are presented in the following. The analysis considers an example fixed BS state, $x_{\text{BS}} = -5$ m, $y_{\text{BS}} = 0$ m, $\alpha_{\text{BS}} = 0$ deg, fixed UE state, $x_{\text{UE}} = 5$ m, $y_{\text{UE}} = 0$ m, $\alpha_{\text{UE}} = 90$ deg, $b_{\text{UE}} = 0$ ns, while the locations of the single-bounce and double-bounce IPs are bounded within the interval $x_n, y_n \in [-10$ m, 10 m] $\forall n$. It is assumed that the

⁴Let us consider an example with linearization point $\hat{\mathbf{x}}^{(j)} = [(\hat{\mathbf{s}}^{(j)})^{\top}, (\hat{\mathbf{m}}_1^{(j)})^{\top}, (\hat{\mathbf{m}}_2^{(j)})^{\top}, (\hat{\mathbf{m}}_3^{(j)})^{\top}, (\hat{\mathbf{m}}_4^{(j)})^{\top}]^{\top}$ and double-bounce path with IPs $\hat{\mathcal{M}}_i^{(j)} = \{\hat{\mathbf{m}}_2^{(j)}, \hat{\mathbf{m}}_4^{(j)}\}$. The measurement model for $i \in \mathcal{I}_{\text{DB}}$ is now defined as $\mathbf{h}_i(\hat{\mathbf{x}}^{(j)}) \triangleq \mathbf{h}_i(\hat{\mathbf{s}}^{(j)}, \hat{\mathcal{M}}_i^{(j)})$ and the Jacobian is $\mathbf{H}_i(\hat{\mathbf{x}}^{(j)}) = \begin{bmatrix} \mathbf{H}_i(\hat{\mathbf{s}}^{(j)}) & \mathbf{0}_{d_z \times d_m} & \mathbf{H}_i(\hat{\mathbf{m}}_2^{(j)}) & \mathbf{0}_{d_z \times d_m} & \mathbf{H}_i(\hat{\mathbf{m}}_4^{(j)}) \end{bmatrix}$, in which the partial derivatives $\mathbf{H}_i(\hat{\mathbf{s}}^{(j)})$, $\mathbf{H}_i(\hat{\mathbf{m}}_2^{(j)})$ and $\mathbf{H}_i(\hat{\mathbf{m}}_4^{(j)})$ are given in (43), (44) and (45), respectively.

LoS exists and covariance of the channel parameter estimates is set to $\mathbf{R}_i = ([1 \text{ ns}, 1 \text{ deg}, 1 \text{ deg}]^2) \forall i$, which is the same as used in Section V-B. In the following, we consider two different cases. In *Case 1*, the double-bounce path shares both interaction points with the single-bounce paths, whereas in *Case 2*, the double-bounce path shares the first interaction point with the single-bounce path.

2) *Results and Discussion*: The single-bounce and double-bounce snapshot SLAM performance bounds for *Case 2* are illustrated in Fig. 5. In this figure, the top row presents the PEB, OEB, BEB, and LEB when one LoS and one single-bounce path are available. The bottom row shows the corresponding bounds when a double-bounce path is present, sharing its first IP with the single-bounce path. The LEB for the second IP of the double-bounce path is included in the last column as the double-bounce path introduces an additional IP to the problem. It is evident that the problem geometry has a significant impact on the performance. In fact, the system is rank-deficient if the single-bounce IP is on the line that traverses through the BS and UE, or the second double-bounce IP is on the line segment connecting the first IP and the UE. These regions are illustrated with white lines in the figure and at these locations the problem is intractable since not all of the unknown parameters can be estimated. In such cases, however, it would be advantageous to either try to identify the paths that lead to the degenerate case so that they could be discarded,⁵ or use the Moore-Penrose inverse instead when the system does not have a unique solution. One of the aims of this paper is to highlight such rank-deficient problem geometries and developing robust estimator that can handle these special cases is left for future work. In general, the performance bounds for single- and double-bounce snapshot SLAM are nearly identical, and on average the lower bound decreases only by 3.8% for position, 0% for orientation, 3.2% for clock bias, and 5.0% for the first landmark location when the double-bounce path is available. Thus, the main advantage of the double-bounce path in *Case 2* is that estimation performance can be improved slightly, and that an additional landmark can be estimated which improves situational awareness of the surrounding environment, i.e., the accuracy and completeness of the overall map.

The performance bounds for *Case 1* are illustrated in Fig. 6. In the top row, one LoS path and two single-bounce paths are considered, and the PEB, OEB, BEB, and LEB for the two IPs are shown. In the bottom row, a double-bounce path that shares both IPs with the single-bounce paths is included, and the resulting bounds are presented. The inclusion of the double-bounce path breaks the symmetry properties of the PEB and BEB, as shown in the bottom row. This is due to the difference of the geometry: when the two IPs of the double-bounce path lie in different angular directions with respect to the BS and UE, the path can provide more spatial information compared to the case where both IPs lie along similar directions. As shown, compared to Fig. 5, the second single-bounce path provides additional information, thereby tightening the estimation bounds.

⁵The problem can still have full rank with a subset of paths. As an example, if the double-bounce path is discarded in Fig. 5, the problem can still be solved with the LoS and single-bounce NLoS for which the bounds are illustrated on the top row of the figure.

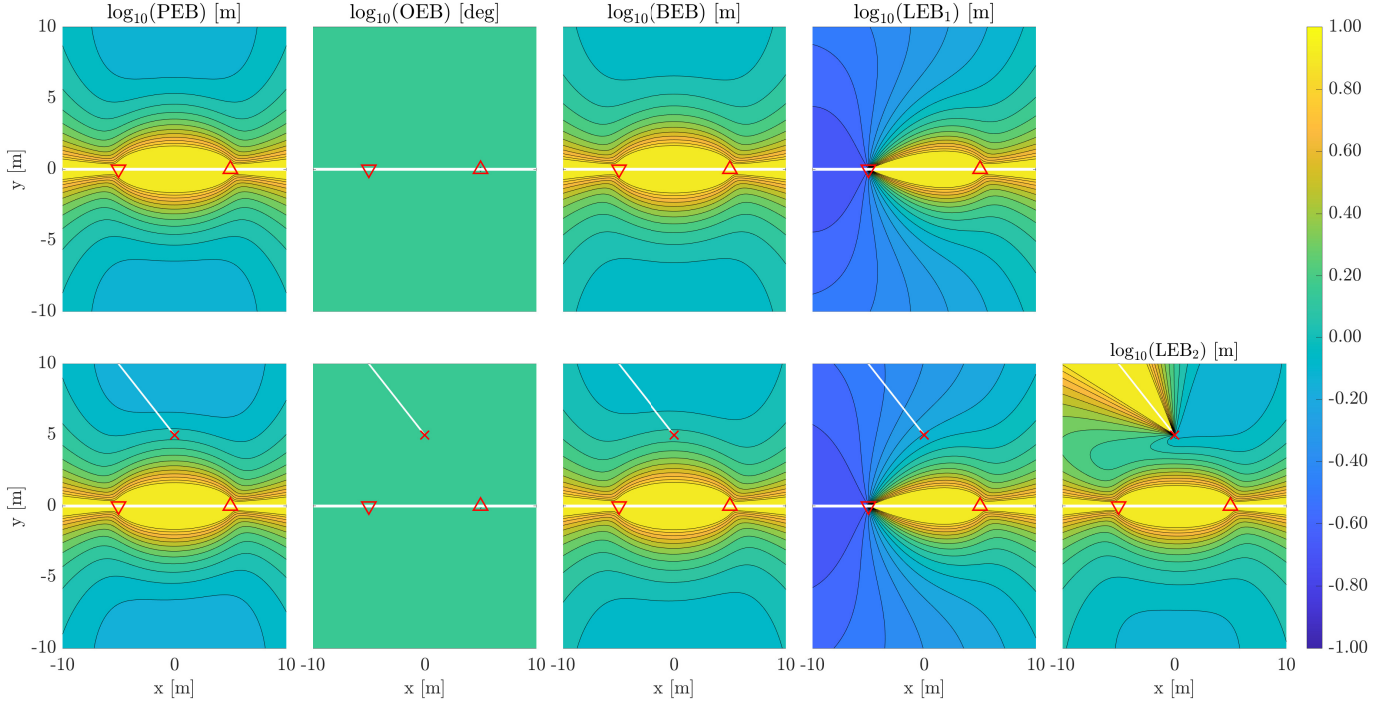


Fig. 5. On top, the performance bounds with LoS and one single-bounce NLoS path. On bottom, the performance bounds with LoS, one single-bounce NLoS and one double-bounce NLoS path, which shares the first interaction point with the single-bounce NLoS path (case 2). In the figures, the IP of the single-bounce NLoS path is varied $x, y \in [-10 \text{ m}, 10 \text{ m}]$, whereas the second IP of the double-bounce NLoS path is fixed to $x = 0 \text{ m}, y = 5 \text{ m}$. The BS location illustrated using (∇) , the UE location with (\triangle) , and the second IP of the double-bounce NLoS path using (\times) .

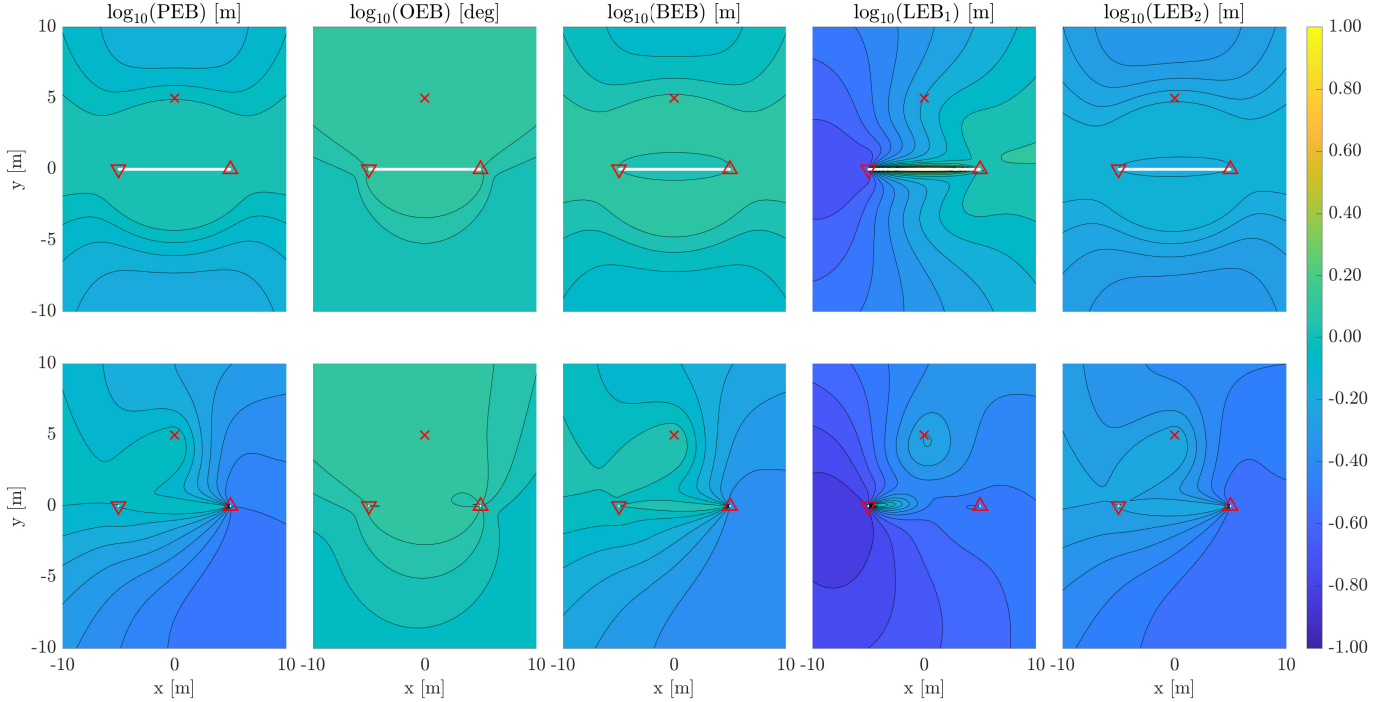


Fig. 6. On top, the performance bounds with LoS and two single-bounce NLoS paths. On bottom, the performance bounds with LoS, two single-bounce NLoS paths and one double-bounce NLoS path, which shares both interaction points with the single-bounce NLoS paths (case 1). In the figures, the IP of one single-bounce NLoS path is varied $x_1, y_1 \in [-10 \text{ m}, 10 \text{ m}]$, whereas the IP of the second single-bounce NLoS path is fixed to $x_2 = 0 \text{ m}, y_2 = 5 \text{ m}$. The double-bounce path propagates as follows: $\text{BS} \rightarrow [x_1, y_1]^T \rightarrow [x_2, y_2]^T \rightarrow \text{UE}$. The BS location illustrated using (∇) , the UE location with (\triangle) , and the IP of the fixed single-bounce NLoS path using (\times) .

Moreover, the double-bounce path provides three additional measurements (i.e., \mathbf{z}_i) which introduce new system constraints without adding any new unknowns (i.e., \mathbf{m}_n). As a result, the double-bounce path further improves the performance bounds,

and on average the lower bound decreases by 36.8% for position, 5.3% for orientation, 35.3% for clock bias, 44.1% for the first landmark location, and 32.3% for the second landmark location when the double-bounce path is available. Such improvements

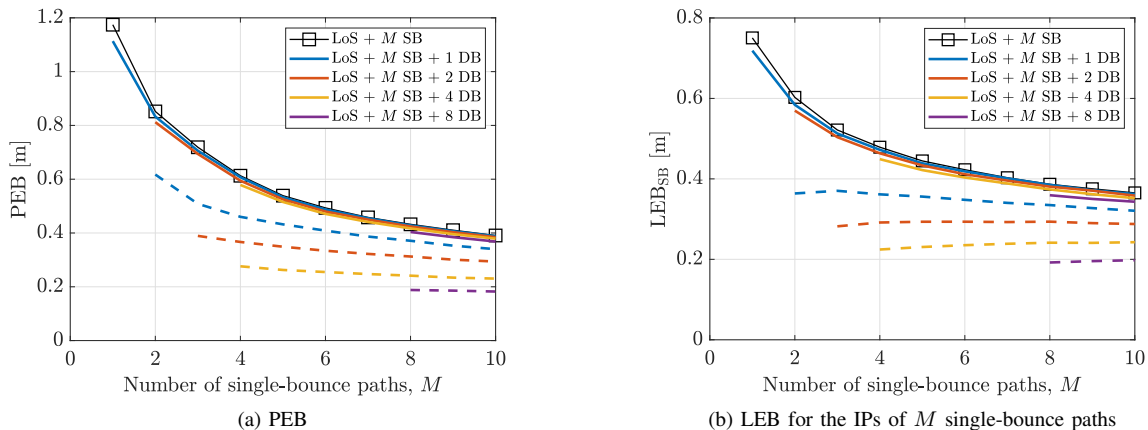


Fig. 7. PEB and LEB_{SB} as a function of number of single-bounce paths (x-axis) and double-bounce paths (illustrated with different colors). In the figures, the scenario where every double-bounce path shares one IP with one of the single-bounce NLoS paths illustrated using solid lines (Case 2), whereas the dashed lines represent the scenario in which every double-bounce path shares both IPs with two different single-bounce NLoS paths (Case 1).

are really notable already. Interestingly, the double-bounce signal also improves identifiability of the system in between the BS and UE, since the x -coordinate of the first IP becomes observable. To conclude, when the double-bounce path shares both of its IPs with the single-bounce IPs, the estimation performance enhances significantly and identifiability of the system also improves.

Thus far, we have only considered a single double-bounce path and at most two single-bounce paths. In Fig. 7, PEB and LEB_{SB} (LEB for the IPs of single-bounce paths) are illustrated as a function of the number of single- and double-bounce paths for two cases. As shown, the bounds are inversely proportional to the number of single-bounce paths, and the accuracy improves as the number of double-bounce paths increases. However, the two cases yield significantly different results. In Case 2, the improvement with respect to the single-bounce only scenario is marginal despite having up to eight double-bounce paths, whereas in Case 1, the performance improves significantly as the number of double-bounce paths increases. Interestingly in Case 1, the performance with three single-bounce paths and two double-bounce paths outperforms a system with ten single-bounce paths. The reason is that every single-bounce path provides three additional known parameters and two additional unknowns, whereas the double-bounce paths do not increase the number of unknown parameters in Case 1. This implies that the double-bounce paths solely create additional constraints to the system which is beneficial in terms of estimation performance.

B. Experimental Results

1) *Experimental Setup*: We evaluate the performance of the proposed and benchmark SLAM algorithms using an open access real-world 60 GHz measurement dataset, collected indoors on the campus of Tampere University [40]. In total, the dataset consist of 45 different UE locations of which 32 were measured in LoS conditions and 13 in NLoS conditions. Beamformed measurements were obtained using 400 MHz transmission bandwidth utilizing 5G NR-specified downlink positioning reference signals. The experimental details and the hardware used are further explained in [2], [40]. For channel measurements, the AoD and AoA are estimated from the beam

reference signal received power measurements using a constant false alarm rate-based detector and the ToA is estimated using the singular value decomposition-based method introduced in [2]. The covariance of the channel parameters is empirically tuned and set to $\mathbf{R}_i = ([1 \text{ ns}, 1 \text{ deg}, 1 \text{ deg}]^2) \forall i$. The angle threshold used to classify double-bounce paths in (25) and (26) is set as $T_\psi = 2 \text{ deg}$, the threshold to terminate the Gauss-Newton algorithm is $T_\epsilon = 0.1$, and the maximum number of allowed Gauss-Newton iterations is $J = 5$.

The proposed snapshot SLAM algorithm is benchmarked with respect to two other snapshot SLAM algorithms. The first benchmark is the robust snapshot SLAM algorithm introduced in [8], which estimates the UE state and landmarks using a LS method. The second benchmark is the SLAM algorithm introduced in [41], which instead applies MLE. Both benchmarks solve the SLAM problem by exploiting only the LoS and single-bounce NLoS paths; all the other measurements, including higher-order NLoS paths are discarded. In this work, we refer to these benchmarks as SB-LS (single-bounce LS) and SB-MLE (single-bounce MLE), respectively. Performance is compared in terms of root mean squared error (RMSE) of the estimated UE position, orientation and clock bias. Ground-truth landmark positions are not available, which is a common problem using real-world experimental data.

2) *Results and Discussion*: Fig. 8 illustrates the sequential operation of the proposed estimator at one example UE position under pure NLoS condition. In the first stage, single-bounce paths are identified and an initial estimate of the UE state together with single-bounce IPs is obtained as explained in Section IV-B. The initial solution of the proposed algorithm, which is essentially the same as SB-LS, is visualized in Fig. 8a. In the example UE position, six single-bounce paths are identified and used to solve the problem. The position, heading and clock bias RMSE of the initial solution are [0.82 m, 2.00 deg, 2.05 ns], respectively. Building on the initial solution, Fig. 8b depicts the classification and estimation of double-bounce paths for which the details are given in Section IV-C. Three double-bounce candidates (dashed lines) are found whose AoDs align with that of existing single-bounce paths (solid lines). Consequently, for all three paths, the IP of the aligned single-bounce path is treated as the first shared IP of

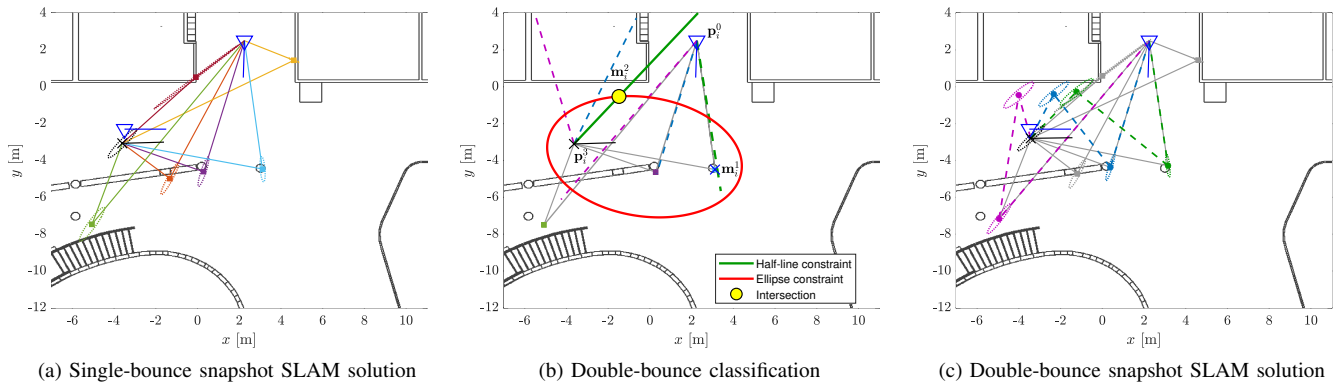


Fig. 8. Illustration at one example UE position when the LoS path does not exist. In the figures, ground truth BS and UE positions are shown using (∇) and UE position estimate using (\times). In the figures, the identified single-bounce paths illustrated using solid lines, double-bounce paths shown using dashed lines, whereas covariances of the UE and IP position estimates visualized with dotted ellipses. In (a), the initial solution is shown which is computed only using the single-bounce paths. Figure (b) illustrates the steps of identifying and determining the double-bounce paths (outliers that are not classified as double-bounce signals are not visualized for clarity). In addition, estimating the second IP is illustrated for one example double-bounce candidate. In (c), the final estimate is shown which is obtained using the proposed double-bounce snapshot SLAM algorithm.

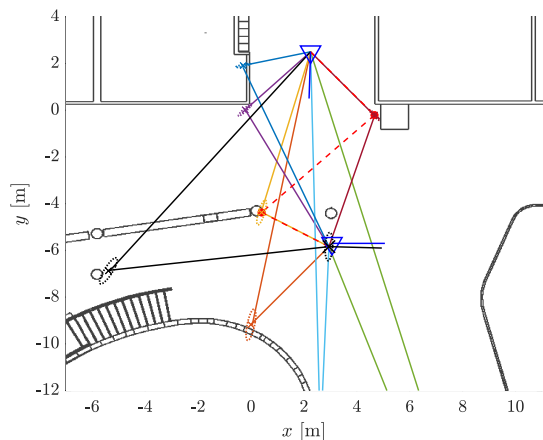


Fig. 9. Illustration of an example snapshot SLAM solution using the proposed algorithm when the double-bounce path shares both IPs with the single-bounce paths (shown using a red dashed line).

the double-bounce candidate. Once this shared IP is determined, the second IP of the double-bounce candidate can be estimated from the measurement constraints as explained in Section IV-D. In the example of Fig. 8b, the second IP of the double-bounce path is estimated as the intersection between an ellipse whose foci are the UE position and the first IP, and a half-line that spans from the UE toward the AoA direction (green solid line). Lastly, both single-bounce and double-bounce paths are jointly exploited to refine the estimates, as shown in Fig. 8c, and as explained in Section IV-E. As illustrated, exploiting the three identified double-bounce paths allows mapping landmarks that are not visible with single-bounce paths alone. In addition, the double-bounce paths improve the accuracy since the position, heading and clock bias RMSE are reduced to [0.50 m, 0.96 deg, 0.87 ns], respectively. Thus, exploiting the double-bounce paths decreases the position, heading and clock error by 0.32 m, 1.04 deg, 1.18 ns, respectively. Moreover, it is observable from the figures that the uncertainties of the UE and existing IP positions estimates are slightly reduced, since each double-bounce path adds information to the UE and shared IPs, consistent with the FIM analysis in Sec. III-D.

Overall, a total of 424 resolvable propagation paths are collected in the 45 UE positions. Among them, the benchmark methods and the initial solution of the proposed algorithm classify the paths as: 32 LoS paths (7.55%), 233 single-bounce paths (54.95%), and the remaining 159 (37.5%) are categorized as multi-bounce paths and clutter. Using the proposed method with angular threshold $T_\psi = 2$ deg, 50 double-bounce NLoS paths are detected among the remaining paths, accounting for 31.45% of the subset. Notably, two of these double-bounce paths share both IPs with existing single-bounce paths. An example of such a case is shown in Fig. 9. In this case, adding the double-bounce path does not introduce any additional unknown parameters compared to SB-MLE. Instead, its measurements directly contribute to refining the estimates of the UE state and the two shared IPs. The position, heading and clock bias RMSE of the benchmark and proposed methods are: [0.26 m, 2.23 deg, 0.90 ns] and [0.18 m, 1.73 deg, 0.59 ns], respectively. Thus, the proposed method improves the UE state estimates by 30.8% for position, 22.4% for orientation, and 34.4% for clock bias, notably larger than the improvements observed when the double-bounce path shares only one IP as we will discuss next.

Fig. 10 visualizes the results over all UE positions, and Table I summarizes the quantitative metrics. Across 45 UE positions, the proposed method identifies a total of 50 double-bounce paths, spread over 32 UE positions, while 2 double-bounce paths are detected that share both IPs with the single-bounce paths. Regarding environmental mapping, the proposed algorithm detects 48 additional landmarks, representing a 21% increase relative to both single-bounce benchmarks. Particularly, double-bounce paths enable mapping of previous unobservable landmarks as illustrated in Fig. 10c. In the figure, green markers highlight additional walls and corners as shown in the upper-left and lower-right regions, that cannot be inferred from single-bounce paths alone. As summarized in Table I, the overall RMSE of the UE state improves by 6.90% for position, 2.98% for orientation, and 10.20% for clock bias compared with SB-MLE, and by 12.90%, 3.74%, and 20.72%, respectively, compared with SB-LS. Moreover, these gains come with no substantial increase in computational complexity since the main

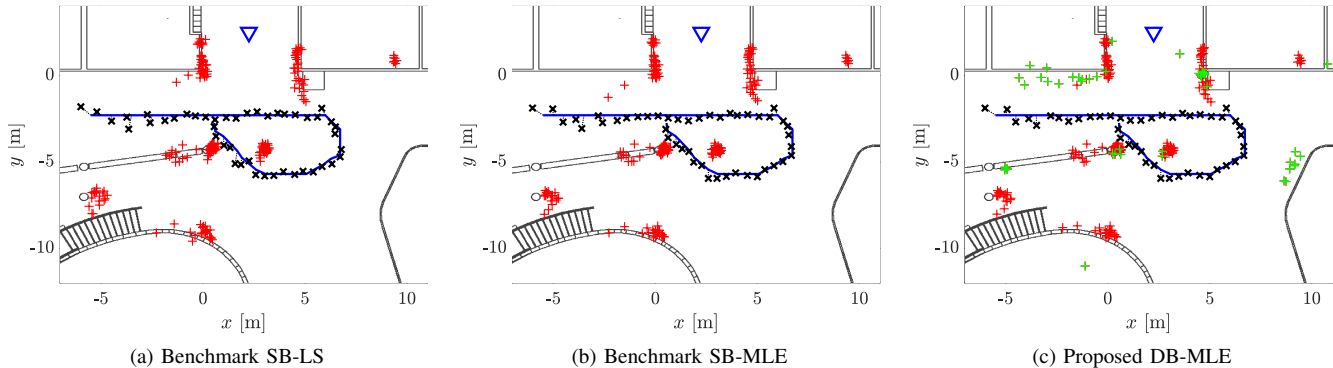


Fig. 10. SLAM performance using the benchmark algorithms and the proposed method. In the figures, BS position is shown using (∇), the ground truth UE trajectory with ($-$), UE position estimates using (\times), single-bounce IP position estimates with ($+$) and double-bounce IP position estimates using ($+$).

TABLE I
RMSE PERFORMANCE COMPARISON OF THE ALGORITHMS IN TERMS OF UE STATE ESTIMATION

Methods	Cond.	Pos. [m]	Head. [deg]	Clk. [ns]	Time [ms]
Proposed		0.22	1.92	0.80	1.79
SB-MLE	LoS (32/45)	0.23	1.91	0.81	0.83
SB-LS		0.25	1.93	0.98	0.65
Proposed		0.35	2.03	1.05	689.17
SB-MLE	NLoS (13/45)	0.41	2.24	1.31	687.54
SB-LS		0.41	2.27	1.40	682.80
Proposed		0.27	1.95	0.88	200.37
SB-MLE	All (45/45)	0.29	2.01	0.98	199.21
SB-LS		0.31	2.03	1.11	197.71

computation burden of the proposed and benchmark algorithms stem from the RANSAC-inspired search to identify single-bounce paths. Overall, the results are inline with the bound analysis conducted in Section V-A which revealed that double-bounce signals improve the performance significantly more when the double-bounce path shares both of its IPs with the single-bounce IPs, compared to a situation where only one of the IPs is shared with a single-bounce IP.

As shown in Table I, in terms of the UE state estimation accuracy, the proposed method achieves average RMSE improvements of [0.03 m, 0.01 deg, 0.17 ns] under LoS conditions and [0.06 m, 0.24 deg, 0.35 ns] under NLoS conditions, with respect to SB-LS. The gains under NLoS conditions are on average higher. This trend is expected because, without a direct LoS path, the UE state is inferred solely from the NLoS paths, which carry more correlated geometric information. Consequently, the benchmark leaves more room for improvement when additional paths are exploited under NLoS conditions. Double-bounce paths contribute to these improvements by coupling the UE state with two IPs, providing additional information. However, the magnitude of the improvement depends on factors such as the geometry at each snapshot and the number of double-bounce paths available.

VI. CONCLUSION

In this article, we addressed the role and potential of double-bounce NLoS paths in snapshot SLAM problem in terms of estimation performance and environmental mapping capabilities. First, we derived and analyzed the FIM and the corresponding estimation CRB of the snapshot SLAM problem with double-bounce paths, and established generic identifiability conditions: the problem is solvable when the double-bounce paths share

at least one IP with existing single-bounce paths. Then, we proposed a new estimator framework and corresponding algorithms to identify double-bounce paths based on geometry consistency and further to solve the snapshot SLAM problem. Numerical results on the bounds show that double-bounce paths sharing one IP yield modest gains, whereas double-bounce paths sharing both IPs provide relatively larger improvements in estimation accuracy. Experimental results with the proposed estimator corroborate and support these fundamental trends: UE estimation accuracy improves in line with the bound analysis. And most importantly, double-bounce paths also enable discovery and localization of new landmarks that are unobservable from single-bounce paths alone, expanding the maps without incurring significant computational overhead. Thus, the proposed methods provide an important step forward for extracting timely and accurate situational awareness of the physical environment, in the spirit of cellular ISAC, towards the 6G networks. Our future work will focus on extending the double-bounce methods to filtering and smoothing-based simultaneous localization and mapping, while also exploring the use of higher-order bounces and paths.

APPENDIX A

MODEL PARAMETERS AND JACOBIANS

The parameters of the model in (3) for LoS, single-bounce NLoS and double-bounce NLoS, as well as the Jacobians $\mathbf{H}_i(\mathbf{s}) = \partial \mathbf{h}_i(\mathbf{s}, \mathcal{M}_i) / \partial \mathbf{s}$ and $\mathbf{H}_i(\mathbf{m}_i) = \partial \mathbf{h}_i(\mathbf{s}, \mathcal{M}_i) / \partial \mathbf{m}_i$ are defined in the following.

1) *LoS*: The signal propagates directly from BS to UE ($\mathcal{M}_i = \emptyset$). The model parameters are $d = \|\mathbf{p}_{\text{BS}} - \mathbf{p}_{\text{UE}}\|$, $[\delta_\phi^x, \delta_\phi^y]^\top = \mathbf{p}_{\text{BS}} - \mathbf{p}_{\text{UE}}$, $[\delta_\theta^x, \delta_\theta^y]^\top = \mathbf{p}_{\text{BS}} - \mathbf{p}_{\text{UE}}$ and the Jacobian is

$$\mathbf{H}_i(\mathbf{s}) = \begin{bmatrix} -\delta_\phi^x/d & -\delta_\phi^y/d & 0 & 1 \\ \delta_\phi^x/d^2 & -\delta_\phi^y/d^2 & 0 & 0 \\ \delta_\theta^x/d^2 & -\delta_\theta^y/d^2 & -1 & 0 \end{bmatrix}. \quad (40)$$

2) *Single-bounce NLoS*: The signal experiences one interaction with the environment ($\mathcal{M}_i = \{\mathbf{m}_i^1\}$). The model parameters are $d = \|\mathbf{p}_{\text{BS}} - \mathbf{m}_i^1\| + \|\mathbf{m}_i^1 - \mathbf{p}_{\text{UE}}\|$, $[\delta_\phi^x, \delta_\phi^y]^\top = \mathbf{p}_{\text{BS}} - \mathbf{m}_i^1$, $[\delta_\theta^x, \delta_\theta^y]^\top = \mathbf{m}_i^1 - \mathbf{p}_{\text{UE}}$ and the Jacobians are

$$\mathbf{H}_i(\mathbf{s}) = \begin{bmatrix} -\delta_\theta^x/d_\theta & -\delta_\theta^y/d_\theta & 0 & 1 \\ 0 & 0 & 0 & 0 \\ \delta_\theta^x/d_\theta^2 & -\delta_\theta^y/d_\theta^2 & -1 & 0 \end{bmatrix}, \quad (41)$$

$$\mathbf{H}_i(\mathbf{m}_i^1) = \begin{bmatrix} \delta_\theta^x/d_\theta - \delta_\phi^x/d_\phi & \delta_\theta^y/d_\theta - \delta_\phi^y/d_\phi \\ \delta_\phi^y/d_\phi^2 & -\delta_\phi^x/d_\phi^2 \\ -\delta_\theta^y/d_\theta^2 & \delta_\theta^x/d_\theta^2 \end{bmatrix}, \quad (42)$$

where $d_\phi = \|\mathbf{p}_{\text{BS}} - \mathbf{m}_i^1\|$ and $d_\theta = \|\mathbf{m}_i^1 - \mathbf{p}_{\text{UE}}\|$.

3) *Double-bounce NLoS*: The signal experiences two interactions with the environment ($\mathcal{M}_i = \{\mathbf{m}_i^1, \mathbf{m}_i^2\}$). The model parameters are $d = \|\mathbf{p}_{\text{BS}} - \mathbf{m}_i^1\| + \|\mathbf{m}_i^2 - \mathbf{m}_i^1\| + \|\mathbf{m}_i^2 - \mathbf{p}_{\text{UE}}\|$, $[\delta_\phi^x, \delta_\phi^y]^\top = \mathbf{p}_{\text{BS}} - \mathbf{m}_i^1$, $[\delta_\theta^x, \delta_\theta^y]^\top = \mathbf{m}_i^2 - \mathbf{p}_{\text{UE}}$, and the Jacobians are

$$\mathbf{H}_i(\mathbf{s}) = \begin{bmatrix} -\delta_\theta^x/d_\theta & -\delta_\theta^y/d_\theta & 0 & 1 \\ 0 & 0 & 0 & 0 \\ \delta_\theta^y/d_\theta^2 & -\delta_\theta^x/d_\theta^2 & -1 & 0 \end{bmatrix}, \quad (43)$$

$$\mathbf{H}_i(\mathbf{m}_i^1) = \begin{bmatrix} \delta_\zeta^x/d_\zeta - \delta_\phi^x/d_\phi & \delta_\zeta^y/d_\zeta - \delta_\phi^y/d_\phi \\ \delta_\phi^y/d_\phi^2 & -\delta_\phi^x/d_\phi^2 \\ 0 & 0 \end{bmatrix}, \quad (44)$$

$$\mathbf{H}_i(\mathbf{m}_i^2) = \begin{bmatrix} \delta_\theta^x/d_\theta - \delta_\zeta^x/d_\zeta & \delta_\theta^y/d_\theta - \delta_\zeta^y/d_\zeta \\ 0 & 0 \\ -\delta_\theta^y/d_\theta^2 & \delta_\theta^x/d_\theta^2 \end{bmatrix}, \quad (45)$$

where $[\delta_\zeta^x, \delta_\zeta^y]^\top = \mathbf{m}_i^1 - \mathbf{m}_i^2$, $d_\zeta = \|\mathbf{m}_i^1 - \mathbf{m}_i^2\|$, $d_\phi = \|\mathbf{p}_{\text{BS}} - \mathbf{m}_i^1\|$ and $d_\theta = \|\mathbf{m}_i^2 - \mathbf{p}_{\text{UE}}\|$.

REFERENCES

- [1] N. González-Prelcic *et al.*, "The integrated sensing and communication revolution for 6G: Vision, techniques, and applications," *Proceedings of the IEEE*, 2024.
- [2] E. Rastorgueva-Foi *et al.*, "Millimeter-wave radio SLAM: End-to-end processing methods and experimental validation," *IEEE Journal on Selected Areas in Communications*, 2024.
- [3] E. Leitinger *et al.*, "A belief propagation algorithm for multipath-based SLAM," *IEEE Transactions on Wireless Communications*, vol. 18, no. 12, pp. 5613–5629, 2019.
- [4] J. Yang *et al.*, "Angle-based SLAM on 5G mmwave systems: Design, implementation, and measurement," *IEEE Internet of Things Journal*, vol. 10, no. 20, pp. 17 755–17 771, 2023.
- [5] M. Lotti *et al.*, "Radio SLAM for 6G systems at THz frequencies: Design and experimental validation," *IEEE Journal of Selected Topics in Signal Processing*, vol. 17, no. 4, pp. 834–849, 2023.
- [6] H. Kim *et al.*, "RIS-enabled and access-point-free simultaneous radio localization and mapping," *IEEE Transactions on Wireless Communications*, vol. 23, no. 4, pp. 3344–3360, 2023.
- [7] H. Premachandra, R. Liu, C. Yuen, and U.-X. Tan, "UWB radar SLAM: An anchorless approach in vision denied indoor environments," *IEEE Robotics and Automation Letters*, vol. 8, no. 9, pp. 5299–5306, 2023.
- [8] O. Kaltiokallio *et al.*, "Robust snapshot radio SLAM," *IEEE Transactions on Vehicular Technology*, pp. 1–6, 2024.
- [9] —, "Integrated snapshot and filtering-based bistatic radio SLAM in mmWave networks," in *Proc. IEEE SPAWC*, 2024, pp. 301–305.
- [10] Y. Zhang and K. Ho, "Multistatic localization in the absence of transmitter position," *IEEE Transactions on Signal Processing*, vol. 67, no. 18, pp. 4745–4760, 2019.
- [11] D. Tagliaferri *et al.*, "Cooperative coherent multistatic imaging and phase synchronization in networked sensing," *IEEE Journal on Selected Areas in Communications*, vol. 42, no. 10, pp. 2905–2921, 2024.
- [12] A. Fascista, A. Coluccia, H. Wymeersch, and G. Seco-Granados, "Downlink single-snapshot localization and mapping with a single-antenna receiver," *IEEE Transactions on Wireless Communications*, vol. 20, no. 7, pp. 4672–4684, 2021.
- [13] Y. Ge *et al.*, "Mmwave mapping and SLAM for 5G and beyond," in *Integrated Sensing and Communications*. Springer, 2023, pp. 445–475.
- [14] —, "A computationally efficient EK-PMBM filter for bistatic mmwave radio SLAM," *IEEE Journal on Selected Areas in Communications*, vol. 40, no. 7, pp. 2179–2192, 2022.
- [15] O. Kaltiokallio *et al.*, "mmwave simultaneous localization and mapping using a computationally efficient EK-PHD filter," in *2021 IEEE Int. Conf. Information Fusion (FUSION)*, 2021, pp. 1–8.
- [16] Y. Ge *et al.*, "Batch SLAM with PMBM data association sampling and graph-based optimization," *IEEE Transactions on Signal Processing*, 2025.
- [17] M. Liang, E. Leitinger, and F. Meyer, "Direct multipath-based SLAM," *IEEE Transactions on Signal Processing*, 2025.
- [18] Y. Ge *et al.*, "5G SLAM using the clustering and assignment approach with diffuse multipath," *Sensors*, vol. 20, no. 16, p. 4656, 2020.
- [19] C. Gentner *et al.*, "Multipath assisted positioning with simultaneous localization and mapping," *IEEE Transactions on Wireless Communications*, vol. 15, no. 9, pp. 6104–6117, 2016.
- [20] K. Witrissal *et al.*, "High-accuracy localization for assisted living: 5G systems will turn multipath channels from foe to friend," *IEEE Signal Processing Magazine*, vol. 33, no. 2, pp. 59–70, 2016.
- [21] H. Kim *et al.*, "PMBM-based SLAM filters in 5G mmwave vehicular networks," *IEEE Transactions on Vehicular Technology*, vol. 71, no. 8, pp. 8646–8661, 2022.
- [22] Z. Li, F. Jiang, H. Wymeersch, and F. Wen, "An iterative 5G positioning and synchronization algorithm in NLOS environments with multi-bounce paths," *IEEE Wireless Communications Letters*, vol. 12, no. 5, pp. 804–808, 2023.
- [23] C. Ling, X. Yin, H. Wang, and R. S. Thomä, "Experimental characterization and multipath cluster modeling for 13–17 GHz indoor propagation channels," *IEEE Transactions on Antennas and Propagation*, vol. 65, no. 12, pp. 6549–6561, 2017.
- [24] S. Ju, Y. Xing, O. Kanhere, and T. S. Rappaport, "Millimeter wave and sub-terahertz spatial statistical channel model for an indoor office building," *IEEE Journal on Selected Areas in Communications*, vol. 39, no. 6, pp. 1561–1575, 2021.
- [25] A. Guerra, F. Guidi, and D. Dardari, "Single-anchor localization and orientation performance limits using massive arrays: MIMO vs. beamforming," *IEEE Transactions on Wireless Communications*, vol. 17, no. 8, pp. 5241–5255, 2018.
- [26] A. Shahmansoori *et al.*, "Position and orientation estimation through millimeter-wave MIMO in 5G systems," *IEEE Transactions on Wireless Communications*, vol. 17, no. 3, pp. 1822–1835, 2017.
- [27] R. Mendrzik, H. Wymeersch, G. Bauch, and Z. Abu-Shaban, "Harnessing NLOS components for position and orientation estimation in 5G millimeter wave MIMO," *IEEE Transactions on Wireless Communications*, vol. 18, no. 1, pp. 93–107, 2018.
- [28] A. Kakkavas, M. H. C. Garcia, R. A. Stirling-Gallacher, and J. A. Nossek, "Performance limits of single-anchor millimeter-wave positioning," *IEEE Transactions on Wireless Communications*, vol. 18, no. 11, pp. 5196–5210, 2019.
- [29] Z. Zhou, H. Chen, G. Steinböck, and H. Wymeersch, "Digital twin-assisted high-precision massive MIMO localization in urban canyons," *arXiv preprint arXiv:2511.20453*, 2025.
- [30] B. Hu *et al.*, "Multipath identification, user localization, and environment mapping in radio SLAM," *IEEE Transactions on Communications*, vol. 72, no. 10, pp. 6457–6473, 2024.
- [31] O. Kaltiokallio *et al.*, "Bistatic mmwave mapping in obstructed environments using double-bounce signals," in *Proc. IEEE SPAWC*, 2024, pp. 106–110.
- [32] Y. Liu, L. Wu, X. Cai, and M. B. Shankar, "Graph-based multi-bounce modeling and channel parameter estimation for indoor sensing," *IEEE Transactions on Wireless Communications*, 2025.
- [33] E. Leitinger, A. Venus, B. Teague, and F. Meyer, "Data fusion for multipath-based SLAM: Combining information from multiple propagation paths," *IEEE Transactions on Signal Processing*, vol. 71, pp. 4011–4028, 2023.
- [34] X. Li, B. J. Deuschmann, E. Leitinger, and F. Meyer, "Adaptive multipath-based SLAM for distributed MIMO systems," *arXiv preprint arXiv:2506.21798*, 2025.
- [35] M. Koivisto *et al.*, "Channel parameter estimation and TX positioning with multi-beam fusion in 5G mmwave networks," *IEEE Transactions on Wireless Communications*, vol. 21, no. 5, pp. 3192–3207, 2021.
- [36] H. L. Van Trees, *Detection, Estimation, and Modulation Theory, Part I: Detection, Estimation, and Linear Modulation Theory*. John Wiley & Sons, 2004.
- [37] H. Wymeersch *et al.*, "5G mmWave downlink vehicular positioning," in *2018 IEEE Global Communications Conference*, 2018, pp. 206–212.
- [38] S. M. Kay, *Fundamentals of Statistical Signal Processing: Estimation Theory*. Prentice Hall, 1993.
- [39] S. Boyd, "Convex Optimization," *Cambridge UP*, 2004.
- [40] E. Rastorgueva-Foi *et al.*, "Millimeter-Wave radio SLAM: 60 GHz indoor sensing dataset," 2024. [Online]. Available: <https://dx.doi.org/10.21227/xskh-dk87>
- [41] X. Zhang *et al.*, "Robust and efficient Bayesian approach for snapshot radio SLAM," in *2025 International Conference on Localization and GNSS (ICL-GNSS)*, 2025, pp. 1–7.